# The Radial Distribution and Excitation of H₂ around Young Stars in the HST-ULLYSES Survey

Kevin France[1] ⬤, Nicole Arulanantham[2] ⬤, Erin Maloney[1], P. Wilson Cauley[1] ⬤, P. Ábrahám[3,4,5] ⬤, Juan M. Alcalá[6] ⬤,
Justyn Campbell-White[7] ⬤, Eleonora Fiorellino[6] ⬤, Gregory J. Herczeg[8,9] ⬤, Brunella Nisini[10] ⬤, and Miguel Vioque[11,12] ⬤

[1] Laboratory for Atmospheric and Space Physics, University of Colorado Boulder, Boulder, CO 80303, USA; kevin.france@colorado.edu
[2] Space Telescope Science Institute, 3700 San Martin Drive, Baltimore, MD 21218, USA
[3] Konkoly Observatory, Research Centre for Astronomy and Earth Sciences, Eötvös Loránd Research Network (ELKH), Konkoly-Thege Miklós út 15-17, 1121 Budapest, Hungary
[4] CSFK, MTA Centre of Excellence, Konkoly Thege Miklós út 15-17., H-1121 Budapest, Hungary
[5] ELTE Eötvös Loránd University, Institute of Physics, Pázmány Péter sétány 1/A, H-1117 Budapest, Hungary
[6] INAF-Osservatorio Astronomico di Capodimonte, via Moiariello 16, I-80131 Napoli, Italy
[7] European Southern Observatory, Karl-Schwarzschild-Strasse 2, D-85748 Garching bei München, Germany
[8] Kavli Institute for Astronomy and Astrophysics, Peking University, Beijing 100871, People's Republic of China
[9] Department of Astronomy, Peking University, Beijing 100871, People's Republic of China
[10] INAF—Osservtorio Astronomico di Roma. Via di Frascati 33, I-00078 Monte Porzio Catone, Italy
[11] Joint ALMA Observatory, Alonso de Córdova 3107, Vitacura, Santiago 763-0355, Chile
[12] National Radio Astronomy Observatory, 520 Edgemont Road, Charlottesville, VA 22903, USA

## Abstract

The spatial distribution and evolution of gas in the inner 10 au of protoplanetary disks form the basis for estimating the initial conditions of planet formation. Among the most important constraints derived from spectroscopic observations of the inner disk are the radial distributions of the major gas phase constituents, how the properties of the gas change with inner disk dust evolution, and how the chemical abundances and excitation conditions are influenced by the high-energy radiation from the central star. We present a survey of the radial distribution, excitation, and evolution of inner disk molecular hydrogen (H₂) obtained as part of the Hubble Space Telescope-ULLYSES program. We analyze far-UV spectroscopy of 71 (63 accreting) pre-main-sequence systems in ULLYSES DR5 to characterize the H₂ emission lines, H₂ dissociation continuum emission, and major photochemical/disk evolution driving the UV emissions (Lyα, UV continuum, and C IV). We use the widths of the H₂ emission lines to show that most fluorescent H₂ arises between 0.1 and 1.4 au from the parent star, and show positive correlations of the average emitting radius with the accretion luminosity and with the dust disk mass. We find a strong correlation between H₂ dissociation emission and both the accretion-dominated Lyα luminosity and the inner disk dust clearing, painting a picture where water molecules in the inner 3 au are exposed to and dissociated by strong Lyα emission as the opacity of the inner disk declines with time.

## 1. Introduction

The circumstellar environments in which planets form are dynamic and volatile places. Mass accretion onto the central stars is active and rapid stellar rotation drives strong magnetic fields. These processes power high levels of UV and X-ray emission, as well as temporal variability that alters the physical state and longevity of the protoplanetary disk. The stellar high-energy radiation (UV and X-ray) controls circumstellar disk dispersal (Alexander et al. 2014; Pascucci et al. 2022), strongly influencing the final stages of planet formation. Young stars complete their mass assembly at the same time as protoplanets are forming around these objects (1–10 Myr; Haisch et al. 2001; Fedele et al. 2010; Ribas et al. 2014), therefore, there is strong competition between dynamical disk clearing through forming protoplanets (e.g., Rice et al. 2003; Dodson-Robinson & Salyk 2011; van der Marel et al. 2018) and disk dispersal through photoevaporation and disk winds, which depend on the

strength and shape of the pre-main-sequence far-ultraviolet (FUV; 912–1800 Å) radiation field (Alexander et al. 2014; Ercolano & Owen 2016; Ercolano & Pascucci 2017; Wang & Goodman 2017). The high-energy radiation produced in the accretion region and surrounding shock-heated gas is responsible for the high levels of UV continuum and line radiation from classical T Tauri stars (CTTSs; Ingleby et al. 2011; France et al. 2014b; Schneider et al. 2020).

Current studies of the accretion of circumstellar disk material onto young stars explore the competing processes of magnetorotational instability (MRI) and magnetohydrodynamic (MHD) disk winds for removing excess angular momentum from the disk and allowing material to accrete onto the central protostar. In the MRI scenario, gas within ∼0.1 au is ionized by the central star and entrained in the stellar magnetic field (Balbus & Hawley 1991), while the MHD disk wind picture proposes that outflowing gas from the disk surface at radii out to tens of astronomical units (see, e.g., Lesur 2021 for a recent review) removes angular momentum from the disk. Ultimately, material is funneled onto the central star along field lines where it creates an accretion shock at (possibly) several contact points with the pre-main-sequence photosphere

(Calvet & Gullbring 1998; Muzerolle et al. 2001; Hartmann et al. 2016; Pittman et al. 2022). The final phase of mass accretion (stellar ages of 2–10 Myr) is particularly important as accretion luminosity and stellar activity catalyze the dispersal and chemistry of the protoplanetary disk, impacting the timescales for planet formation and the accretion of protoplanetary atmospheres (Wang & Goodman 2017).

The high-energy radiation from the accretion region is also responsible for ionizing and photodissociating inner disk atoms and molecules, catalyzing disk surface chemistry, and driving many of the observable signatures of the inner regions of the disk. Molecular gas emission and absorption originating inside of 10 au provide our best means of estimating the conditions at the radii where gas giant and rocky planet cores are forming and accreting their nascent atmospheres. Surveys of molecular emission from the inner few astronomical units provide constraints on the radial distribution, temperature, and composition of planet-forming inner disks. Surveys of mid-IR emission from CO (Salyk et al. 2009; Brown et al. 2013; Banzatti & Pontoppidan 2015; Banzatti et al. 2022), $H_2O$ and organic molecules (Pontoppidan et al. 2010; Salyk et al. 2011b; Carr & Najita 2011; Banzatti et al. 2023), UV emission and absorption of $H_2$ and CO (Herczeg et al. 2004; France et al. 2011; Schindhelm et al. 2012; France et al. 2014a; Arulanantham et al. 2021), and spectrally/spatially resolved near-IR observations (Carmona et al. 2011; Pontoppidan et al. 2011; Brittain et al. 2015) have placed constraints on the relative abundance ratios of $H_2$, CO, and $H_2O$, the evolution of the inner gas disk radius, and the excitation conditions of the molecular gas. The inventory of disk molecules and photochemical studies of the planet-forming environments around young stars is expected to expand rapidly in the era of JWST (Öberg & Bergin 2021; Grant et al. 2023; Kóspál et al. 2023).

$H_2$ is the primary mass component of gas-rich disks, however, the lack of an intrinsic dipole moment and large energy spacing between the rotational levels have traditionally made direct detection of the rovibrational emission lines of the molecule challenging to study in a large number of disks (although see, e.g., Carmona et al. 2011; Gangi et al. 2020; Kóspál et al. 2023). Conversely, the electronic excitation spectrum of $H_2$ is among the brightest features in the UV spectra of pre-main-sequence stars (France et al. 2012), and can serve as a diagnostic of weak mass accretion when traditional accretion diagnostics (e.g., H$\alpha$ and near-UV Balmer continuum) do not provide clear evidence of active accretion (Ingleby et al. 2011; Alcalá et al. 2019).

The molecular tracers observed at UV wavelengths are primarily excited by UV fluorescence and dissociation. Fluorescent $H_2$ (Herczeg et al. 2002) emission is detected in the circumstellar environments of all accreting protostars surveyed to date (e.g., France et al. 2012) and is a sensitive probe of remnant gas in disks with evolved dust opacity (Hoadley et al. 2015). Fluorescent CO emission is observed in a fraction of disks, with an observed bias toward disks that show dust clearing in their mid-IR spectral slopes (Schindhelm et al. 2012; Arulanantham et al. 2021). $H_2$ dissociation continuum emission (the "1600 Å Bump"), where Ly$\alpha$ photons dissociate water and the resultant, highly nonthermal $H_2$ dissociation products, is observed in almost all dust-evolved disks (France et al. 2017); however, only approximately a third of "full" or "primordial" disks display

this feature. Together, the fluorescent $H_2$ line emission and continuum bump trace both the radial distributions and UV irradiation of hot molecular gas in the inner disks.

In this paper, we present a new survey of the $H_2$ features observed in the UV spectra of CTTSs, taking advantage of the Ultraviolet Legacy Library of Young Stars as Essential Standards (ULLYSES) program. ULLYSES obtained almost 500 orbits of UV spectroscopic observations with the Hubble Space Telescope (HST), targeting approximately 71 new accreting and nonaccreting young stars. We analyze the ULLYSES Data Release 5 (DR5) to provide the largest spectral catalog of $H_2$ line and continuum features obtained to date to understand better the radial distribution and evolution of the inner disk molecules around young stars.

This paper is laid out as follows: Section 2 presents an overview of the ULLYSES FUV spectra analyzed here and Section 3 presents the emission line measurements and a publicly available data catalog of the FUV line parameters. Section 3 concludes with the derivation of the Ly$\alpha$ luminosity, average $H_2$ fluorescent emitting radius, and the properties of the FUV continuum radiation. In Section 4, we discuss how these results suggest a physical picture where stellar/accretion photons have greater penetration depth and drive greater molecular dissociation as the dust opacity of the inner disk declines. We conclude with a brief summary in Section 5.

## 2. Archival FUV Spectra from ULLYSES

We analyze FUV spectra obtained as part of the 487 HST orbits in the low-mass-star portion of ULLYSES (see Roman-Duval et al. 2020 for a program overview). The observations include data acquired through DR5[13] with the addition of five targets observed in summer 2022. The final sample (Table 1) is primarily composed of accreting T Tauri stars observed as part of the ULLYSES program, however, the DR5 catalog includes a number of stars from previous young star observing programs with similar observational plans (see, e.g., Ardila et al. 2013; France et al. 2017). The final source list analyzed here includes 63 accreting and eight nonaccreting sources.

The target sample presented in ULLYSES DR5 were obtained between late 2009 and mid 2022 with the HST Cosmic Origins Spectrograph (COS; Green et al. 2012). As the data collection strategy and analysis of FUV spectra of accreting protostars has been discussed extensively in previous works (France et al. 2012; Roman-Duval et al. 2020), we present a high-level overview of the data set here with an emphasis on the FUV spectral line catalog creation in Section 3. The FUV spectral reduction and analysis follow the general description from the ODYSSEUS program overview paper (Espaillat et al. 2022), and we refer the reader to that work for an example of the FUV spectra analyzed in the context of the larger ODYSSEUS panchromatic analysis program. We also employ mid-IR spectral slopes (12–22 $\mu$m) from Wide-field Infrared Survey Explorer (WISE) photometry (Cutri et al. 2013). The WISE data were downloaded from the NASA IPAC Infrared Science Archive, and WISE observations with data quality flags ($cc\_flags \neq 0$) were excluded from the analysis. In addition, visual inspection of the WISE images indicated potential field crowding or extended emission in CVSO-90, CVSO-107, CVSO-176, RECX-15 (ET Cha, echa-j0843.3-7915), and CS Cha. Of these, we note that

---

[13] https://ullyses.stsci.edu/ullyses-download.html

**Table 1**
ULLYSES DR5 Target Parameters

| Name | $M_*$ ($M_\odot$) | $\dot{M}_{acc}$ ($10^{-8} M_\odot$ yr$^{-1}$) | $i$ (deg) | $d$ (pc) | $A_V$ (mag) | WISE W3 (mag) | WISE W4 (mag) | References |
|---|---|---|---|---|---|---|---|---|
| 2MASSj04390163+2336029 | 0.17 | 0.04 | ... | 126 | 0.00 | ... | ... | 14, 15 |
| 2MASSj11432669-7804454 | 0.14 | 0.19 | ... | 153 | 0.40 | 8.676 | 7.052 | 1 |
| CHX18n | 0.81 | 0.47 | 56 | 192 | 0.80 | 5.560 | 3.584n | 1, 29 |
| CVSO-17 | 0.37 | 0.00 | ... | 414 | 0.00 | 11.130 | 8.932 | 7 |
| CVSO-36 | 0.39 | 0.00 | ... | 335 | 0.10 | 10.306 | 8.593 | 7 |
| CVSO-58 | 0.81 | 0.43 | ... | 349 | 0.80 | 7.000 | 4.905 | 7 |
| CVSO-90 | 0.62 | 0.25 | ... | 338 | 0.10 | 7.622 | 5.345 | 7 |
| CVSO-104 | 0.37 | 0.32 | 43 | 360 | 0.20 | 7.560 | 5.571 | 7, 20 |
| CVSO-107 | 0.53 | 5.01 | ... | 330 | 0.30 | 7.419 | 5.128 | 7 |
| CVSO-109 | 0.46 | 3.24 | ... | 400 | 0.10 | 6.523 | 4.527 | 7 |
| CVSO-146 | 0.86 | 0.27 | ... | 332 | 0.60 | 7.072 | 4.597 | 7 |
| CVSO-165 | 0.84 | 0.08 | ... | 400 | 0.20 | 6.571 | 4.626 | 7 |
| CVSO-176 | 0.25 | 1.45 | ... | 302 | 1.00 | 7.896 | 6.221 | 7 |
| echa-j0843-7915 (RECX-15) | 0.20 | 0.08 | 60 | 103 | 0.00 | ... | ... | 4, 5, 27 |
| echa-j0844-7833 | 0.07 | 0.00 | ... | 98 | 0.50 | ... | ... | 4, 5 |
| LkCa-4 | 0.77 | 0.00 | ... | 129 | 0.69 | 8.038 | 7.934 | 9, 10 |
| LkCa-15 | 0.85 | 0.13 | 49 | 157 | 0.60 | 5.696 | 3.565 | 11, 3, 19 |
| LkCa-19 | 1.35 | 0.00 | ... | 157 | 0.00 | 7.972 | 7.109 | 9 |
| HN5 | 0.18 | 0.28 | ... | 195 | 1.10 | 5.864 | 4.371 | 1 |
| RECX-1 | 0.75 | 0.00 | ... | 98 | 0.00 | 7.058 | 6.943 | 4, 5 |
| RECX-11 | 0.83 | 0.02 | 70 | 99 | 0.10 | 5.388 | 3.718 | 4, 5, 27 |
| RXJ0438.6+1556 | 1.20 | 0.03 | ... | 139 | 0.30 | 8.154 | 8.122 | 13 |
| RXJ1556.1-3655 | 0.50 | 1.20 | 53 | 158 | 1.00 | 6.268 | 3.887 | 16, 30 |
| SSTC2dj160000-422158 | 0.19 | 0.06 | 65 | 159 | 0.10 | ... | ... | 16, 29 |
| SSTC2dj160830-382827 | 1.40 | 0.11 | 72 | 153 | 0.20 | ... | ... | 16, 17 |
| SSTC2dj161243-381503 | 0.44 | 0.17 | 43 | 159 | 0.80 | ... | ... | 16, 30 |
| SSTC2dj161344-373646 | 0.16 | 0.11 | 54 | 158 | 0.60 | ... | ... | 16, 29 |
| Sz 19 | 2.08 | 2.34 | 45 | 189 | 1.50 | 3.011 | 1.057 | 1, 29 |
| Sz 45 | 0.56 | 0.51 | 43 | 189 | 0.70 | 6.948 | 4.156 | 1, 29 |
| Sz 66 | 0.29 | 0.05 | 40 | 156 | 1.00 | 6.363 | 4.432 | 6, 29 |
| Sz 68 | 1.40 | 0.58 | 32 | 152 | 1.00 | 2.896 | 0.856 | 16, 30 |
| Sz 69 | 0.20 | 0.03 | 35 | 155 | 0.00 | 5.614 | 4.420 | 6, 28 |
| Sz 71 | 0.37 | 0.11 | 40 | 156 | 0.70 | 5.716 | 3.671 | 6, 28 |
| Sz 72 | 0.37 | 0.95 | 53 | 156 | 1.00 | 5.987 | 3.911 | 6, 28 |
| Sz 75 | 0.82 | 6.79 | ... | 152 | 1.00 | 4.342 | 2.379 | 16 |
| Sz 76 | 0.22 | 0.07 | ... | 159 | 0.30 | 7.366 | 5.274 | 16 |
| Sz 77 | 0.75 | 0.07 | ... | 155 | 0.30 | 5.362 | 3.437 | 16 |
| Sz 84 | 0.16 | 0.06 | 75 | 155 | 0.00 | 9.115 | 6.340 | 6, 29 |
| Sz 97 | 0.23 | 0.03 | 73 | 157 | 0.00 | 7.749 | 4.976 | 6, 29 |
| Sz 98 | 0.70 | 5.89 | 46 | 156 | 1.00 | 3.986 | 2.097 | 16, 29 |
| Sz 99 | 0.23 | 0.04 | ... | 158 | 0.00 | 7.847 | 6.009 | 6 |
| Sz 100 | 0.16 | 0.04 | 47 | 141 | 0.00 | 6.486 | 4.517 | 6, 29 |
| Sz 102 | 0.24 | 0.08 | 53 | 160 | 1.13 | 6.196 | 3.382 | 16, 29 |
| Sz 103 | 0.22 | 0.10 | 50 | 157 | 0.70 | 6.940 | 4.843 | 6, 29 |
| Sz 104 | 0.16 | 0.02 | 57 | 159 | 0.00 | 7.438 | 4.806 | 6, 29 |
| Sz 110 | 0.22 | 0.30 | 32 | 157 | 0.00 | 6.307 | 4.116 | 6, 29 |
| Sz 111 | 0.58 | 0.09 | 54 | 158 | 0.50 | 8.922 | 5.731 | 6, 29 |
| Sz 114 | 0.21 | 0.11 | 6 | 153 | 0.30 | 5.721 | 3.380 | 6, 29 |
| Sz 117 | 0.26 | 0.25 | 47 | 156 | 0.50 | 7.169 | 4.884 | 16, 29 |
| Sz 129 | 0.79 | 0.40 | 31 | 160 | 0.90 | 5.722 | 3.597 | 16, 29 |
| Sz 130 | 0.36 | 0.15 | 36 | 159 | 0.40 | 6.530 | 4.514 | 6, 28 |
| AA Tau | 0.80 | 0.33 | 59 | 134 | 0.50 | 4.645 | 2.505 | 11, 3, 18 |
| CE Ant | 0.46 | 0.00 | ... | 34 | 0.00 | 6.598 | 5.998 | 3 |
| CS Cha | 1.05 | 1.20 | 37 | 168 | 0.80 | 7.095 | 2.758 | 2, 3, 13, 19 |
| DE Tau | 0.59 | 2.64 | 34 | 128 | 0.60 | 4.895 | 2.725 | 11, 3, 21 |
| DK Tau | 0.71 | 3.79 | 58 | 140 | 0.80 | 3.599 | 1.800 | 11, 3, 22 |
| DM Tau | 0.50 | 0.29 | 35 | 144 | 0.00 | 7.085 | 3.571 | 2, 3, 24 |
| DN Tau | 0.60 | 0.35 | 35 | 128 | 1.90 | 5.166 | 3.039 | 11, 3, 23 |
| DR Tau | 0.80 | 3.16 | 5 | 193 | 0.48 | 3.008 | 1.066 | 11, 3, 30 |
| HN Tau | 0.85 | 0.13 | 50 | 140 | 0.50 | 4.174 | 2.160 | 11, 3, 31 |
| IN Cha | 0.19 | 0.05 | ... | 193 | 0.20 | 7.218 | 5.316 | 1 |
| IP Tau | 0.68 | 0.08 | 35 | 129 | 0.20 | 5.436 | 3.578 | 11, 3, 31 |
| MY Lup | 1.06 | 0.02 | 72 | 157 | 1.30 | 5.164 | 2.833 | 16, 26 |
| RY Lup | 1.71 | 1.00 | 68 | 153 | 0.40 | 3.647 | 1.404 | 16, 19 |

**Table 1**
(Continued)

| Name | $M_*$ ($M_\odot$) | $\dot{M}_{acc}$ ($10^{-8}\,M_\odot\,yr^{-1}$) | $i$ (deg) | $d$ (pc) | $A_V$ (mag) | WISE W3 (mag) | WISE W4 (mag) | References |
|---|---|---|---|---|---|---|---|---|
| SY Cha | 0.78 | 0.04 | 51 | 180 | 0.50 | 5.435 | 3.212 | 1, 29 |
| TX Ori | 1.09 | 6.17 | … | 385 | 0.40 | 5.101 | 3.083 | 8 |
| UX Tau A | 1.30 | 1.00 | 35 | 140 | 0.20 | 5.710 | 2.176 | 12, 19 |
| V397 Aur | 0.70 | 0.00 | … | 165 | 0.20 | 7.854 | 6.743 | 9 |
| XX Cha | 0.29 | 0.10 | … | 192 | 0.30 | 5.751 | 3.569 | 1 |
| V505 Ori | 0.81 | 0.30 | … | 392 | 1.00 | 6.564 | 4.539 | 8 |
| V510 Ori | 0.76 | 0.58 | … | 390 | 0.10 | 5.598 | 3.258 | 8 |

**Note.** References for the stellar masses, reddening, accretion rates, and disk inclination: (1) Manara et al. (2017b), (2) Furlan et al. (2009), (3) Ingleby et al. (2013), (4) Rugel et al. (2018), (5) Luhman (2004), (6) Alcalá et al. (2014), (7) Calvet et al. (2005), (8) Maucó et al. (2016), (9) Kenyon & Hartmann (1995), (10) Donati et al. (2014) (11) Furlan et al. (2011) (12) Costigan et al. (2014), (13) Manara et al. (2017a), (14) Slesnick et al. (2006), (15) Herczeg & Hillenbrand (2008), (16) Alcalá et al. (2017), (17) van der Marel et al. (2018), (18) Loomis et al. (2017), (19) Francis & van der Marel (2020), (20) Frasca et al. (2021), (21) Simon et al. (2019), (22) Nelissen et al. (2023), (23) Long et al. (2019), (24) Kudo et al. (2018), (25) Kurtovic et al. (2018), (26) Huang et al. (2018), (27) Lawson et al. (2004), (28) Ansdell et al. (2016), (29) Hendler et al. (2020), (30) Braun et al. (2021), and (31) Simon et al. (2017).
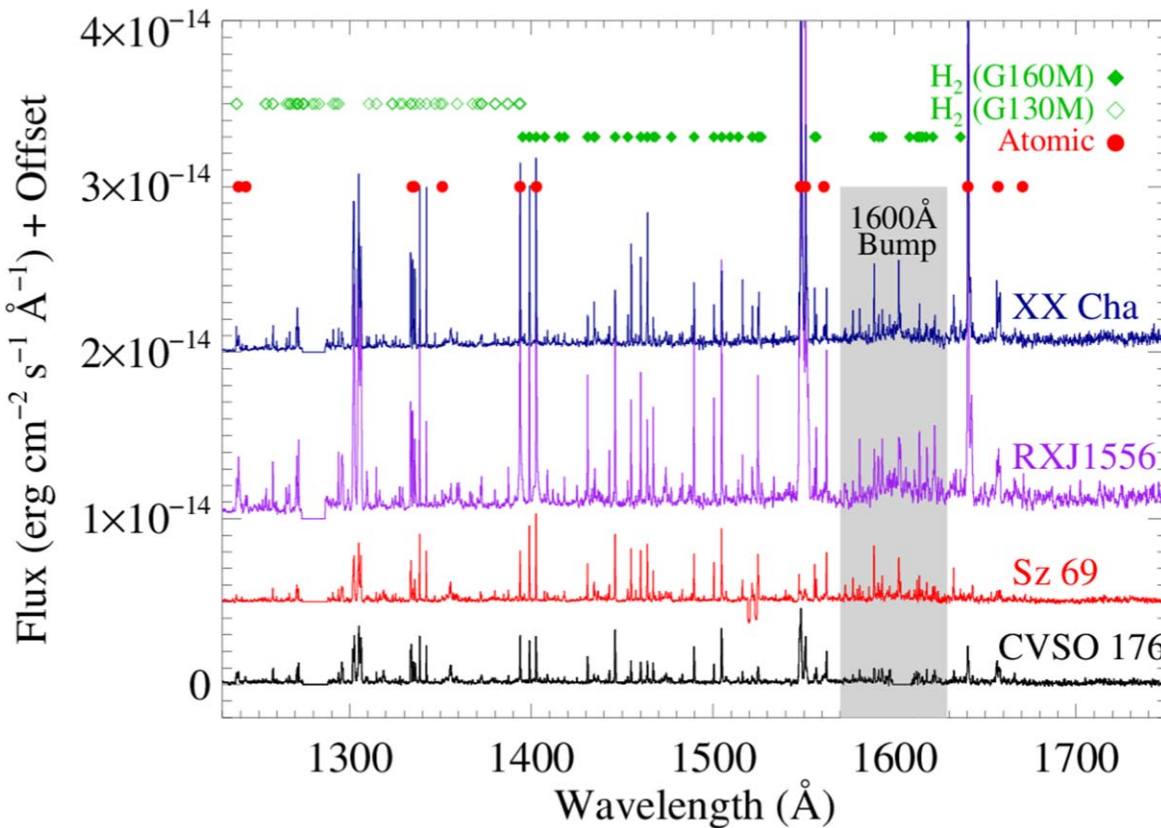


**Figure 1.** Example HST/COS spectra of four representative CTTSs from the ULLYSES survey. The stellar spectra are color coded and labeled in the legend in the lower left; offsets were applied to Sz 69 ($5 \times 10^{-15}$ erg cm$^{-2}$ s$^{-1}$ Å$^{-1}$), RXJ1556.1-3655 (the flux was divided by 2 and an offset of $5 \times 10^{-15}$ erg cm$^{-2}$ s$^{-1}$ Å$^{-1}$ was applied), and XX Cha ($20 \times 10^{-15}$ erg cm$^{-2}$ s$^{-1}$ Å$^{-1}$). Three resolution element (21 pixel) boxcar smoothing has been applied for plotting the full spectral range. The wavelengths of prominent emission lines of H$_2$ (green diamonds, separated by lines that are primarily recorded in the G130M or G160M modes) and atomic lines (red circles) are indicated. The peak wavelength region of the 1600 Å Bump emission from Ly$\alpha$ dissociated H$_2$ (originating from a Ly$\alpha$ dissociated H$_2$O parent population) is indicated by the gray shaded region. The HST/COS observations of CVSO-176 used a single central wavelength setting which results in an $\approx$12–15 Å gap in the spectra where the COS detector segments a and b meet.

CS Cha hosts a well-studied transition disk (Espaillat et al. 2007) providing confidence in the large WISE W3 − W4 color for this source.

The HST observations were made using the COS G130M and G160M grating modes. Most observing programs employed multiple central wavelength settings at several focal-plane split positions to create continuous FUV spectra from ~1140 to 1760 Å and mitigate the effects of fixed pattern noise.[14] These modes provide a point-source resolution between $\Delta v \approx$ 17–22 km s$^{-1}$ with 6–7 pixels per resolution

---

[14] We note that some of the ULLYSES observations used a single central wavelength setting which results in $\approx$12–15 Å gaps in the spectra where the COS detector segments a and b meet.
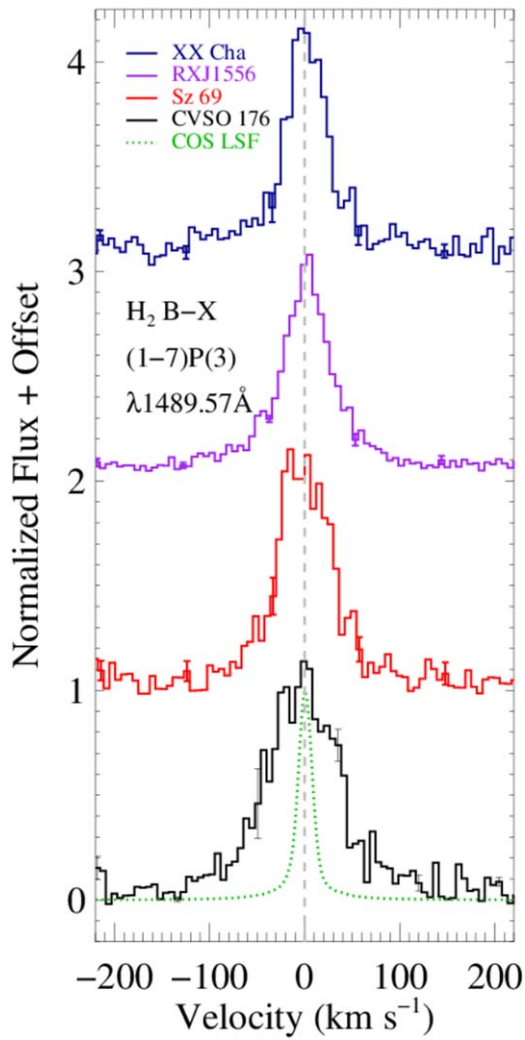
**Figure 2.** Individual H$_2$ $B^1\Sigma_u^+ - X^1\Sigma_g^+$ (1–7) R(3) ($\lambda_{\rm lab}$= 1489.57 Å) emission lines for the four example targets from Figure 1. The spectra are shifted to their rest wavelength for comparison and normalized by the average flux in the peak ($\pm 10$ km s$^{-1}$) of the emission line and offset by 1.0. The HST/COS line-spread function (LSF) is shown as the dotted green line; all emission lines are well resolved in the COS data, indicating kinematic line broadening.

element (Osterman et al. 2011). The total FUV exposure times were between two and 16 orbits per target, depending on the intrinsic luminosity and the interstellar plus circumstellar reddening on the sightline.

We present an example of four representative T Tauri star spectra from ULLYSES in Figure 1 (XX Cha, RXJ1556.1-3655, Sz 69, and CVSO-176). These stars come from a variety of star-forming regions sampled by ULLYSES (Chamaeleon I, Corona Australis, Lupus, and Orion OB1) and the locations of prominent molecular and atomic features in the spectra are shown. As this work focuses primarily on the line and continuum emission from H$_2$, Figures 2 and 3 present representative samples of these features. Figure 2 shows a representative, isolated, fluorescent emission line of H$_2$ ($B^1\Sigma_u^+ - X^1\Sigma_g^+$ (1–7) R(3); $\lambda_{\rm lab}$ = 1489.57 Å) for the four stars shown in Figure 1. Figure 3 presents the range of H$_2$ continuum spectra observed in ULLYSES DR5: the top panel shows the underlying FUV spectral continuum (CVSO-109) showing no molecular emission (see also Espaillat et al. 2022) while the middle panel shows the same spectral extraction from a source
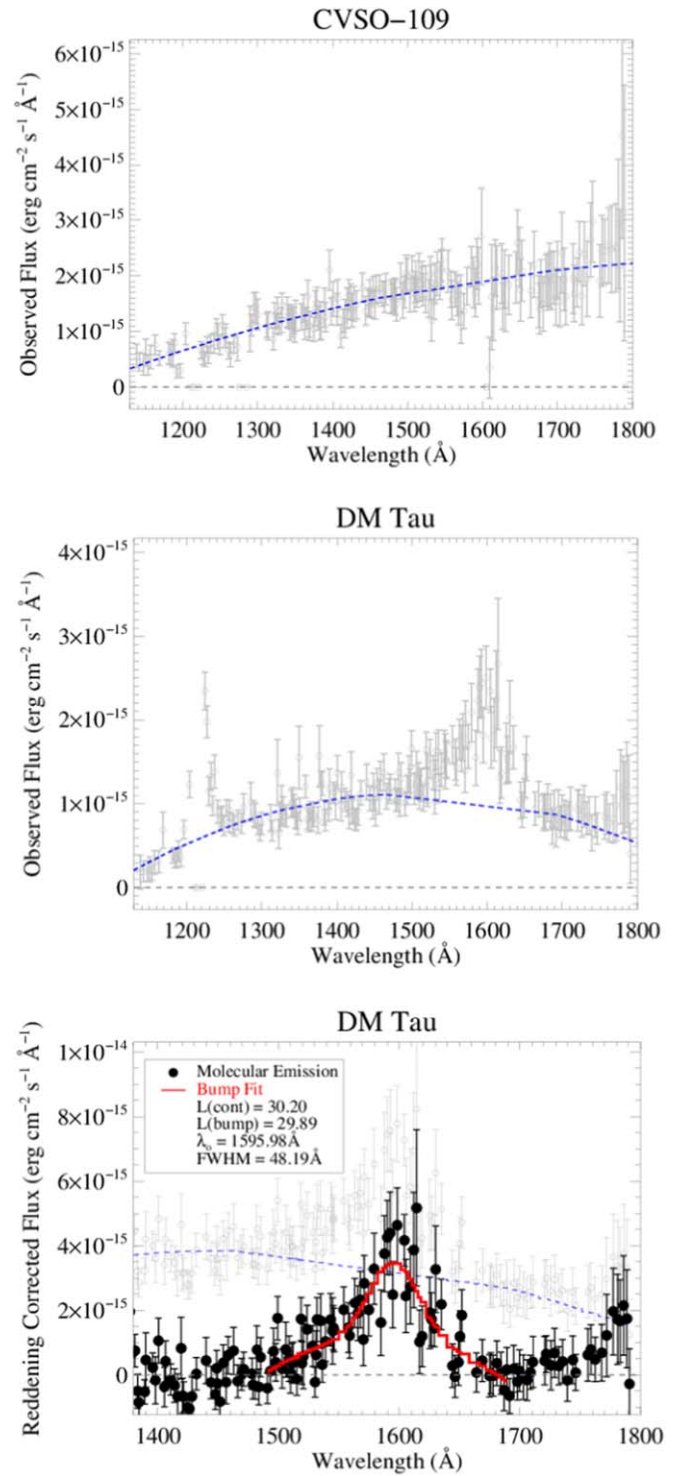


**Figure 3.** Example FUV continuum spectra for two targets in ULLYSES DR5: CVSO-109 (top panel; Espaillat et al. 2022) and DM Tau (center panel). The underlying accretion continuum (fit with a polynomial; blue dashed line) is removed and the residual molecular continuum is shown as the black circle data points in the bottom panel. The molecular continuum fit is parameterized by a Gaussian+polynomial (France et al. 2017) and is shown in red. Molecular continuum fit parameters are shown in the legend; the log$_{10}$(luminosity) of the FUV continuum and the 1600 Å Bump, in units of erg s$^{-1}$, are presented as $L$(cont) and $L$(bump), respectively.

with a strong molecular continuum feature ("1600 Å Bump;" France et al. 2017; DM Tau). The bottom panel of Figure 3 shows the extracted H$_2$ molecular continuum from DM Tau (see Section 3.3).

## 3. FUV Spectral Line Data Reduction and Analysis

We analyzed the brightest FUV lines in the COS spectra: five progressions of fluorescent $H_2$ ([1, 7], [1, 4], [0, 1], [0, 2], and [2, 12]) and hot gas emission from Si III (1206 Å), N V (1238 Å and 1243 Å), Si IV (1394 Å and 1403 Å), and C IV (1548 Å and 1550 Å). The $H_2$ lines are marked in Figure 1, depending on whether they were recorded with the G130M (open diamonds) or G160M (filled diamonds) grating and the hot gas lines are marked with red circles. The spectra and tables of line flux measurements are publicly available in machine-readable format.[15] For each star, we take the high-level processed data from the ULLYSES *cspec.fits files and extract individual emission line flux and error regions, which are saved as line-specific arrays. For hot gas doublets (e.g., C IV, N V, and Si IV), the lines are extracted separately into the blue and red doublet components. Individual extracted emission line regions and tables of line measurements for the ensemble of stars are available on the web portal.

Each array is processed with a 5 pixel boxcar smoothing algorithm to suppress noise without compromising significant kinematic information (all of the emission lines studied here are well resolved; see, e.g., France et al. 2012; Figure 2). The HST/COS LSF contributes ~10%–20% for lines narrower than 40 km s$^{-1}$ and less for broader lines. For each emission line region, the background continuum flux is calculated from an immediately adjacent spectral region then subtracted out from the entire flux array. In Table 2, we present the integrated fluxes measured over the interval ±200 km s$^{-1}$.

The FWHM was calculated nonparametrically to account for the various non-Gaussian shapes of some of the emission lines (Ardila et al. 2013). The brightest 7 pixels (approximately one resolution element) in an emission line region are averaged to find the maximum flux, $F_{max}$. The line center is defined as the average wavelength within the 7 pixel $F_{max}$ region. The half maximum value, $F_{max/2}$ is calculated as

$$F_{max/2} = (F_{max} - F_{cont})/2 + F_{cont}, \qquad (1)$$

where $F_{cont}$ is the value of the continuum emission near the line of interest. The ±half-width points are the wavelengths corresponding to $F_{max/2}$; the difference of these half-width points are the FWHMs presented in Table 2. For the hot gas doublets the FWHM was only calculated for the blue component of the doublet because these doublets are governed by the same physical creation mechanism and the blue components of the doublet are stronger (brighter). Uncertainties on the FWHM are computed using the same method, with the ±1σ flux error added to the flux values to evaluate the minimum and maximum values achievable within the photometric flux uncertainties.

In certain instances (approximately 5% of line profile measurements), the FWHM calculation returned values that did not match a qualitative inspection of the data, and for these lines, we measured the line profiles following the method described by France et al. (2012), where a Gaussian line shape is forward-modeled and compared to the data using a Levenberg–Marquardt least-squares minimization to return the best-fit emission line parameters. This "patch" was tested against approximately a dozen emission lines with good nonparametric results, and the agreement in FWHM and flux

was found to be within 10%–20% in all cases. The emission line measurement files are stored as comma separated value arrays and are publicly available.[16] Each data file includes the emission line IDs, the peak wavelength of each line, the integrated flux of the line, the error on that integrated flux, the FWHM of the line, the error on that FWHM, and a data quality flag. The data quality flags note special circumstances or indicate when there is no emission line. In the following subsections, we describe how these basic data products were used to derive system parameters of the ULLYSES targets (Sections 3.1 and 3.2) and how the FUV continua were extracted from the HST/COS data sets (Section 3.3).

### 3.1. $H_2$ Progression and Lyα Luminosity from the ULLYSES Sample

The fluorescent $H_2$ lines observed in the CTTS sample can be used to constrain the spatial distribution of $H_2$ in the circumstellar environment. For our line profile analysis, we focus on the measurement of four progressions ([$v'$, $J'$] = [1, 7], [1, 4], [0, 1], and [0, 2]). These progressions are pumped through the (1–2)$R$(6) $\lambda_{lab}$ 1215.73 Å, (1–2)$P$(5) $\lambda_{lab}$ 1216.07 Å, (0–2)$R$(0) $\lambda_{lab}$ 1217.21 Å, and (0–2)$R$(1) $\lambda_{lab}$ 1217.64 Å absorbing transitions, respectively.[17] The absorbing transitions are within +14 to +487 km s$^{-1}$ of the Lyα line center. We target the brightest two, unblended emission lines from each progression for analysis here. The $H_2$ emission line centroids are broadly consistent with the stellar radial velocities within the 15 km s$^{-1}$ accuracy of the HST/COS wavelength solution, and we will explore multiple emission line components (e.g., Arulanantham et al. 2018) and their kinematic signatures in a future work.

The emission line fluxes are corrected for interstellar reddening using the $A_V$ values given in Table 1. It has been shown that the dust properties of the Taurus star-forming region differ from the Milky Way average extinction curve (Calvet et al. 2004). However, the shape of the extinction curve for star-forming regions and individual targets remains highly uncertain (McJunkin et al. 2016), and the $A_V$ values derived for individual targets carry significant uncertainties (Carvalho & Hillenbrand 2022; Pittman et al. 2022). Both of these issues are exacerbated by the strong wavelength dependence of the dust attenuation curve, where the reddening correction at 1500 Å has a ~6× larger amplitude relative to 6500 Å for $A_V = 1$. In light of these uncertainties, we adopt a typical interstellar curve (Cardelli et al. 1989) and an $R_V = 3.1$. If, on the other hand, we would have adopted a standard interstellar curve with $R_V = 5.5$ (for $A_V = 1$), the resultant fluxes would be between 20%–40% of the values reported here.

The total flux from a progression $m$ is given by

$$F_m(H_2) = \frac{1}{2}\sum\left(\frac{F_{mn}}{B_{mn}}\right), \qquad (2)$$

where $F_{mn}$ is the reddening-corrected, integrated $H_2$ emission line flux from rovibrational state $m$ (=[$v'$, $J'$]) in the $B^1\Sigma_u^+$

---

**Table 2**
ULLYSES FUV Measurements

| Name | $L(H_2)$ $(10^{29}$ erg s$^{-1})$ | $L(Ly\alpha)$ $(10^{29}$ erg s$^{-1})$ | $L(C$ IV$)$ $(10^{29}$ erg s$^{-1})$ | $L(1600$ Å Bump$)$ $(10^{29}$ erg s$^{-1})$ | $L(FUV$ Cont$)$ $(10^{29}$ erg s$^{-1})$ | FWHM$(H_2)_{[1, 4]}$ (km s$^{-1}$) | FWHM$(H_2)_{[0, 1]}$ (km s$^{-1}$) | $<R(H_2)>_{[1, 4]}$ (au) | $<R(H_2)>_{[0, 1]}$ (au) |
|---|---|---|---|---|---|---|---|---|---|
| 2MASSj04390163+2336029 | 0.05 ± 0.01 | 2.89 | 0.02 | ⋯ | 0.1 | 76.4 ± 17.3 | 13.4 ± 29.0 | 0.08 ± 0.02 | 2.52 ± 5.46 |
| 2MASSj11432669-7804454 | 2.20 ± 0.22 | 61.18 | 0.65 | 0.49 ± 0.28 | 3.6 | 61.7 ± 14.8 | 67.0 ± 4.5 | 0.10 ± 0.02 | 0.08 ± 0.01 |
| CHX18n | 17.65 ± 2.75 | 348.59 | 8.38 | ⋯ | 36.8 | 51.8 ± 4.9 | 49.1 ± 4.5 | 0.75 ± 0.07 | 0.83 ± 0.08 |
| CVSO-17 | 0.04 ± 0.07 | 15.01 | 0.17 | ⋯ | 4.2 | ⋯ | ⋯ | ⋯ | ⋯ |
| CVSO-36 | 0.11 ± 0.09 | 11.62 | 0.09 | ⋯ | 2.8 | ⋯ | ⋯ | ⋯ | ⋯ |
| CVSO-58 | 37.82 ± 3.82 | 817.71 | 21.69 | 10.30 ± 10.00 | 277.6 | 54.3 ± 2.5 | 44.7 ± 4.4 | 0.73 ± 0.03 | 1.08 ± 0.11 |
| CVSO-90 | 16.74 ± 1.74 | 423.96 | 10.30 | ⋯ | 79.1 | 51.8 ± 4.9 | 51.7 ± 1.6 | 0.62 ± 0.06 | 0.62 ± 0.02 |
| CVSO-104 | 8.66 ± 0.69 | 258.39 | 4.14 | ⋯ | 51.8 | 49.3 ± 2.5 | 53.7 ± 4.2 | 0.25 ± 0.01 | 0.21 ± 0.02 |
| CVSO-107 | 15.21 ± 2.49 | 388.81 | 7.94 | ⋯ | 136.0 | 64.1 ± 7.4 | 53.6 ± 13.4 | 0.34 ± 0.04 | 0.49 ± 0.12 |
| CVSO-109 | 14.60 ± 1.52 | 407.72 | 12.72 | ⋯ | 229.5 | 44.4 ± 2.5 | 40.7 ± 3.0 | 0.62 ± 0.03 | 0.74 ± 0.05 |
| CVSO-146 | 28.78 ± 4.50 | 645.24 | 15.46 | ⋯ | 310.0 | 51.8 ± 19.7 | 53.6 ± 6.7 | 0.85 ± 0.32 | 0.80 ± 0.10 |
| CVSO-165 | 11.39 ± 2.00 | 335.04 | 5.63 | ⋯ | 66.2 | 76.4 ± 2.5 | 53.6 ± 13.4 | 0.38 ± 0.01 | 0.78 ± 0.19 |
| CVSO-176 | 51.99 ± 5.58 | 990.56 | 10.54 | ⋯ | 245.9 | 74.0 ± 2.5 | 46.9 ± 2.2 | 0.12 ± 0.00 | 0.30 ± 0.01 |
| echa-j0843-7915 | 5.33 ± 0.48 | 104.36 | 0.48 | 0.96 ± 0.15 | 5.5 | 49.3 ± 2.5 | 55.8 ± 2.2 | 0.22 ± 0.01 | 0.17 ± 0.01 |
| echa-j0844-7833 | 0.15 ± 0.06 | 6.21 | 0.21 | ⋯ | 0.7 | ⋯ | ⋯ | ⋯ | ⋯ |
| LkCa-4 | 0.07 ± 0.30 | 3.45 | 1.50 | ⋯ | 2.3 | ⋯ | ⋯ | ⋯ | ⋯ |
| LkCa-15 | 23.78 ± 3.11 | 405.89 | 12.40 | ⋯ | 50.5 | 51.8 ± 2.5 | 53.6 ± 2.2 | 0.64 ± 0.03 | 0.60 ± 0.02 |
| LkCa-19 | 0.08 ± 0.08 | 4.31 | 0.71 | ⋯ | 1.8 | ⋯ | ⋯ | ⋯ | ⋯ |
| HN5 | 2.52 ± 0.35 | 75.19 | 0.41 | ⋯ | 5.4 | 133.2 ± 93.7 | 17.9 ± 2.2 | 0.03 ± 0.02 | 1.50 ± 0.19 |
| RECX-1 | −0.10 ± 0.13 | 0.07 | 0.51 | ⋯ | 2.3 | ⋯ | ⋯ | ⋯ | ⋯ |
| RECX-11 | 2.07 ± 0.26 | 48.42 | 2.35 | 0.44 ± 0.16 | 5.1 | 61.6 ± 2.5 | 65.9 ± 2.0 | 0.69 ± 0.03 | 0.60 ± 0.02 |
| RXJ0438.6+1556 | 0.06 ± 0.10 | 3.10 | 1.01 | ⋯ | 2.7 | 182.5 ± 88.8 | 78.2 ± 67.0 | 0.10 ± 0.05 | 0.52 ± 0.45 |
| RXJ1556.1-3655 | 105.72 ± 9.49 | 1323.61 | 53.50 | ⋯ | 116.5 | 56.6 ± 2.5 | 49.1 ± 2.2 | 0.36 ± 0.02 | 0.48 ± 0.02 |
| SSTC2dj160000-422158 | 0.14 ± 0.01 | 6.88 | 0.02 | ⋯ | 0.5 | 61.6 ± 2.5 | 35.7 ± 20.1 | 0.15 ± 0.01 | 0.44 ± 0.25 |
| SSTC2dj160830-382827 | 4.83 ± 0.75 | 113.89 | 1.28 | ⋯ | 6.6 | 46.8 ± 2.5 | 40.2 ± 20.1 | 2.06 ± 0.11 | 2.79 ± 1.39 |
| SSTC2dj161243-381503 | 7.63 ± 0.46 | 166.38 | 3.83 | 0.82 ± 0.52 | 14.0 | 54.3 ± 4.9 | 42.4 ± 2.2 | 0.25 ± 0.02 | 0.41 ± 0.02 |
| SSTC2dj161344-373646 | 2.17 ± 0.51 | 61.26 | 4.84 | ⋯ | 13.2 | 49.3 ± 2.5 | 35.7 ± 13.4 | 0.16 ± 0.01 | 0.30 ± 0.11 |
| Sz 19 | 8.29 ± 1.69 | 190.54 | 13.98 | ⋯ | 42.1 | 49.3 ± 9.9 | 41.3 ± 4.5 | 1.44 ± 0.29 | 2.05 ± 0.22 |
| Sz 45 | 21.74 ± 1.96 | 408.30 | 8.43 | ⋯ | 66.8 | 46.8 ± 2.5 | 42.4 ± 2.2 | 0.43 ± 0.02 | 0.53 ± 0.03 |
| Sz 66 | 17.24 ± 1.59 | 313.71 | 0.11 | 2.64 ± 1.45 | 11.9 | 44.4 ± 7.4 | 44.7 ± 2.2 | 0.22 ± 0.04 | 0.22 ± 0.01 |
| Sz 68 | 15.88 ± 2.39 | 291.37 | 8.66 | 3.74 ± 2.37 | 30.3 | 59.2 ± 12.3 | 58.1 ± 6.7 | 0.42 ± 0.09 | 0.43 ± 0.05 |
| Sz 69 | 1.69 ± 0.21 | 49.80 | 0.03 | 0.50 ± 0.21 | 1.1 | 54.3 ± 4.9 | 42.4 ± 2.2 | 0.08 ± 0.01 | 0.13 ± 0.01 |
| Sz 71 | 6.71 ± 0.74 | 148.76 | 2.58 | 1.25 ± 0.78 | 10.8 | 46.9 ± 2.5 | 38.0 ± 4.4 | 0.25 ± 0.01 | 0.38 ± 0.04 |
| Sz 72 | 11.27 ± 1.98 | 224.08 | 14.26 | ⋯ | 65.0 | 56.7 ± 9.9 | 45.4 ± 1.9 | 0.26 ± 0.05 | 0.41 ± 0.02 |
| Sz 75 | 162.14 ± 25.70 | 1826.48 | 73.94 | ⋯ | 966.3 | 78.9 ± 4.9 | 60.3 ± 6.7 | 0.35 ± 0.02 | 0.61 ± 0.07 |
| Sz 76 | 1.33 ± 0.14 | 41.62 | 0.27 | ⋯ | 2.3 | 37.0 ± 2.5 | 60.3 ± 13.4 | 0.43 ± 0.03 | 0.16 ± 0.04 |
| Sz 77 | 6.27 ± 0.78 | 140.53 | 2.77 | 1.09 ± 0.92 | 16.7 | 54.3 ± 9.9 | 46.9 ± 64.8 | 0.68 ± 0.12 | 0.91 ± 1.25 |
| Sz 84 | 0.62 ± 0.09 | 22.58 | 0.10 | ⋯ | 0.6 | 44.4 ± 4.9 | 46.9 ± 11.1 | 0.27 ± 0.03 | 0.24 ± 0.06 |
| Sz 97 | 0.29 ± 0.05 | 12.25 | 0.26 | ⋯ | 1.6 | 51.8 ± 2.5 | 105.0 ± 22.4 | 0.28 ± 0.01 | 0.07 ± 0.01 |
| Sz 98 | 28.07 ± 2.34 | 461.61 | 4.79 | 2.32 ± 2.15 | 59.7 | 49.3 ± 2.5 | 44.7 ± 2.2 | 0.54 ± 0.03 | 0.66 ± 0.03 |
| Sz 99 | 0.25 ± 0.05 | 10.95 | 0.41 | ⋯ | 1.7 | 61.5 ± 17.2 | 22.3 ± 58.0 | 0.16 ± 0.05 | 1.23 ± 3.19 |
| Sz 100 | 1.30 ± 0.12 | 39.04 | 0.17 | ⋯ | 1.6 | 46.8 ± 2.5 | 15.8 ± 2.1 | 0.14 ± 0.01 | 1.22 ± 0.17 |
| Sz 102 | 111.34 ± 12.58 | 1386.21 | 44.74 | 10.10 ± 6.69 | 379.8 | 59.1 ± 4.9 | 62.5 ± 2.2 | 0.16 ± 0.01 | 0.14 ± 0.00 |
| Sz 103 | 7.63 ± 0.66 | 165.16 | 0.22 | ⋯ | 27.0 | 49.3 ± 2.5 | 53.6 ± 2.2 | 0.19 ± 0.01 | 0.16 ± 0.01 |
| Sz 104 | 0.14 ± 0.07 | 6.95 | 0.21 | ⋯ | 3.5 | 76.3 ± 27.1 | 136.2 ± 109.4 | 0.07 ± 0.02 | 0.02 ± 0.02 |
| Sz 110 | 2.00 ± 0.35 | 57.43 | 0.72 | ⋯ | 2.5 | 68.9 ± 9.9 | 100.5 ± 29.0 | 0.05 ± 0.01 | 0.02 ± 0.01 |
| Sz 111 | 13.88 ± 1.54 | 265.72 | 3.30 | 4.05 ± 2.31 | 16.6 | 46.8 ± 2.5 | 58.1 ± 6.7 | 0.63 ± 0.03 | 0.41 ± 0.05 |

8

**Table 2**
(Continued)

| Name | $L(H_2)$ $(10^{29}$ erg s$^{-1})$ | $L(Ly\alpha)$ $(10^{29}$ erg s$^{-1})$ | $L(C\ \text{IV})$ $(10^{29}$ erg s$^{-1})$ | $L(1600\ \text{Å Bump})$ $(10^{29}$ erg s$^{-1})$ | $L(\text{FUV Cont})$ $(10^{29}$ erg s$^{-1})$ | FWHM(H$_2$)$_{[1, 4]}$ (km s$^{-1}$) | FWHM(H$_2$)$_{[0, 1]}$ (km s$^{-1}$) | $<R(H_2)>_{[1, 4]}$ (au) | $<R(H_2)>_{[0, 1]}$ (au) |
|---|---|---|---|---|---|---|---|---|---|
| Sz 114 | 12.68 ± 0.97 | 244.59 | 1.51 | ⋯ | 5.6 | 44.3 ± 2.5 | 35.7 ± 2.2 | 0.01 ± 0.00 | 0.01 ± 0.00 |
| Sz 117 | 1.36 ± 0.82 | 42.13 | 2.54 | ⋯ | 8.1 | 73.8 ± 152.6 | 78.1 ± 73.7 | 0.09 ± 0.19 | 0.08 ± 0.08 |
| Sz 129 | 37.69 ± 4.56 | 588.70 | 18.31 | 8.39 ± 1.74 | 190.6 | 51.8 ± 2.5 | 49.1 ± 2.2 | 0.28 ± 0.01 | 0.31 ± 0.01 |
| Sz 130 | 2.28 ± 0.35 | 63.87 | 1.33 | ⋯ | 5.0 | 49.3 ± 2.5 | 42.4 ± 22.3 | 0.19 ± 0.01 | 0.25 ± 0.13 |
| AA Tau | 25.65 ± 2.60 | 403.91 | 2.04 | 2.70 ± 0.41 | 16.6 | 54.2 ± 2.5 | 53.6 ± 2.2 | 0.71 ± 0.03 | 0.73 ± 0.03 |
| CE Ant | 0.00 ± 0.01 | 0.13 | 0.06 | ⋯ | 0.3 | ⋯ | ⋯ | ⋯ | ⋯ |
| CS Cha | 133.10 ± 12.53 | 1632.53 | 0.44 | 27.60 ± 9.81 | 330.3 | 35.6 ± 0.3 | 35.7 ± 2.2 | 1.06 ± 0.01 | 1.06 ± 0.07 |
| DE Tau | 12.17 ± 2.51 | 219.19 | 6.96 | 1.58 ± 0.64 | 40.5 | 59.2 ± 4.9 | 38.0 ± 8.9 | 0.19 ± 0.02 | 0.46 ± 0.11 |
| DK Tau | 23.13 ± 2.96 | 378.29 | 5.64 | 1.33 ± 1.00 | 63.8 | 69.0 ± 7.4 | 35.7 ± 2.2 | 0.03 ± 0.00 | 0.10 ± 0.01 |
| DM Tau | 5.54 ± 0.71 | 123.69 | 1.68 | 7.82 ± 2.41 | 13.6 | 44.5 ± 0.5 | 40.2 ± 4.5 | 0.29 ± 0.00 | 0.36 ± 0.04 |
| DN Tau | 101.03 ± 26.50 | 1171.54 | 259.67 | ⋯ | 2580.2 | 41.9 ± 7.4 | 49.7 ± 3.1 | 0.40 ± 0.07 | 0.29 ± 0.02 |
| DR Tau | 21.79 ± 7.61 | 412.74 | 11.40 | ⋯ | $2.9 \times 10^5$ | 39.4 ± 2.5 | 26.8 ± 13.4 | 0.02 ± 0.00 | 0.04 ± 0.02 |
| HN Tau | 15.87 ± 2.66 | 280.88 | 2.98 | 2.11 ± 0.73 | 50.3 | 64.1 ± 4.9 | 53.6 ± 6.7 | 0.43 ± 0.03 | 0.62 ± 0.08 |
| IN Cha | 0.71 ± 0.08 | 27.38 | 0.04 | ⋯ | 0.8 | 61.7 ± 2.5 | 40.2 ± 15.6 | 0.13 ± 0.01 | 0.31 ± 0.12 |
| IP Tau | 1.08 ± 0.16 | 32.38 | 1.07 | ⋯ | 4.0 | 51.7 ± 4.9 | 53.6 ± 35.7 | 0.30 ± 0.03 | 0.28 ± 0.18 |
| MY Lup | 68.89 ± 5.93 | 941.26 | 19.46 | ⋯ | 111.8 | 39.5 ± 2.5 | 40.2 ± 4.5 | 2.20 ± 0.14 | 2.12 ± 0.24 |
| RY Lup | 10.90 ± 2.18 | 216.77 | 4.02 | 3.33 ± 2.01 | 18.7 | 49.3 ± 2.5 | 42.4 ± 13.4 | 2.15 ± 0.11 | 2.90 ± 0.92 |
| SY Cha | 12.84 ± 1.15 | 264.34 | 2.87 | 6.01 ± 0.81 | 44.5 | 74.0 ± 2.5 | 55.8 ± 4.5 | 0.31 ± 0.01 | 0.55 ± 0.04 |
| TX Ori | 11.38 ± 1.46 | 329.57 | 1.59 | ⋯ | 263.0 | 56.7 ± 2.5 | 40.2 ± 4.5 | 0.90 ± 0.04 | 1.80 ± 0.20 |
| UX Tau A | 8.11 ± 0.59 | 165.18 | 2.29 | 1.10 ± 0.58 | 8.8 | 44.4 ± 2.5 | 44.7 ± 2.2 | 0.77 ± 0.04 | 0.76 ± 0.04 |
| V397 Aur | 0.00 ± 0.05 | 2.22 | 0.45 | ⋯ | 0.4 | ⋯ | ⋯ | ⋯ | ⋯ |
| XX Cha | 8.63 ± 1.09 | 198.02 | 2.72 | ⋯ | 27.6 | 51.8 ± 7.4 | 40.2 ± 2.2 | 0.29 ± 0.04 | 0.48 ± 0.03 |
| V505 Ori | 49.55 ± 4.61 | 1063.19 | 2.93 | ⋯ | 1164.4 | 51.8 ± 4.9 | 38.0 ± 13.4 | 0.80 ± 0.08 | 1.50 ± 0.53 |
| V510 Ori | 25.63 ± 4.81 | 629.94 | 1.62 | 15.50 ± 5.85 | 174.4 | 41.9 ± 4.9 | 42.4 ± 6.7 | 1.15 ± 0.13 | 1.12 ± 0.18 |

electronic state to $n$ ($=[v'', J'']$) in the ground electronic state, $X^1\Sigma_g^+$. $B_{mn}$ is the branching ratio between these two states, and 2 is the number of emission lines measured from a given progression. The measurement errors are typically small, so we take the flux error to be the average error of the individual measurements of $F_m(H_2)$. The dominant systematic error on the measured $H_2$ flux is the correction for interstellar reddening; we do not attempt to account for this uncertainty in the flux and luminosity errors presented below. The total progression luminosity is then $L_m(H_2) = (4\pi d^2)F_m(H_2)$. In Table 2, we present reddening-corrected luminosities for the [1, 4] and [0, 1] progressions. The total $H_2$ luminosity is the sum of the individual progression luminosities. Because we select a finite number of progressions to analyze, this treatment under-estimates the total $H_2$ fluorescent luminosity by an amount that depends on the temperature and spatial distribution of the absorbing $H_2$, as well as the shape of the Ly$\alpha$ pumping spectrum. As these four progressions are the brightest in essentially all CTTSs, we consider this to be a 20%–30% underestimate of the total fluorescent $H_2$ emission (France et al. 2012).

The fluorescent emission lines of $H_2$ can be used to reconstruct the bright Ly$\alpha$ emission line that is the primary excitation source of this gas (Wood et al. 2002; Herczeg et al. 2004; Schindhelm et al. 2012). In order for this process to produce a high-fidelity reconstruction, a sufficient number of $H_2$ progressions, covering the majority of the Ly$\alpha$ pumping profile, must be detected at moderate to high S/N (e.g., Schindhelm et al. 2012; Arulanantham et al. 2018). Ly$\alpha$ reconstructions with a small number of low-S/N progressions leave the shape and integrated flux of the Ly$\alpha$ line poorly constrained (Espaillat et al. 2022). Of the 63 accreting sources analyzed here, the majority are only detected in three or four $H_2$ progressions—54 detections in [1, 4], 41 detections in each [1, 7] and [0, 1], 33 detections in [0, 2], and only three detections in the [2, 12] progression that is often used to constrain the wings of the Ly$\alpha$ line. Therefore, a full Ly$\alpha$ reconstruction cannot be practically applied to the full ULLYSES sample.

In order to provide a uniform estimate for the Ly$\alpha$ luminosity for ULLYSES, we fit $F(H_2)$ versus $F(Ly\alpha)$ relation using the 14 higher-S/N targets reconstructed by Schindhelm et al. (2012) and $H_2$ fluorescence data from France et al. (2012). These data are shown as the orange points in Figure 4. We extrapolated the ULLYSES measurements of $L(H_2)$ described above onto this relation to estimate the Ly$\alpha$ fluxes for all 63 accreting stars in our sample

$$\log_{10}(F(Ly\alpha)) = m_{Ly\alpha}(\log_{10}(F(H_2))) + b_{Ly\alpha}, \quad (3)$$

where the best-fit coefficients are $m_{Ly\alpha} = 0.791 \pm 0.033$ and $b_{Ly\alpha} = -1.297 \pm 0.400$. Propagating the uncertainties on the fit coefficients of the $F(H_2)$ versus $F(Ly\alpha)$ relation indicates a maximum uncertainty on the associated Ly$\alpha$ luminosities of $\lesssim 40\%$. The small dispersion seen in the extrapolated Ly$\alpha$ luminosities is due to the conversion of the flux–flux relationship from France et al. (2012) to luminosity. We caution that while the original Ly$\alpha$-to-$H_2$ relationship from France et al. (2012) spans approximately 1.5 orders of magnitude in $L(H_2)$, we are extrapolating that relationship to over three orders of magnitude for the present sample. Figure 5 illustrates a comparison of the estimated Ly$\alpha$ to C IV luminosity between



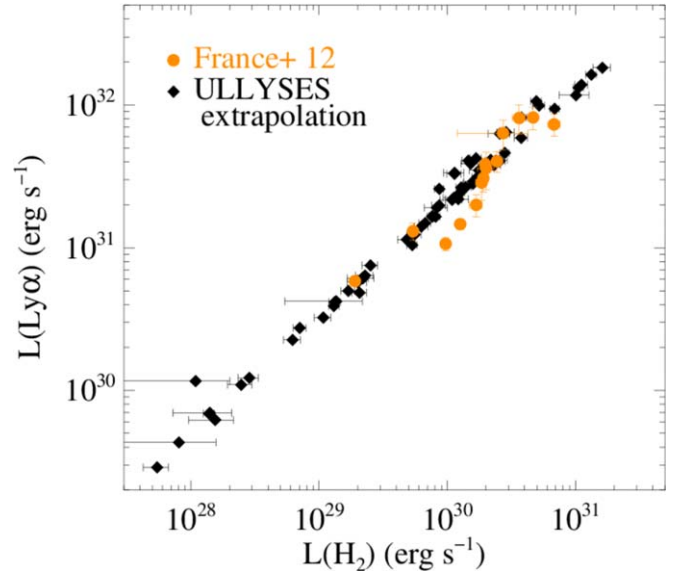**Figure 4.** Projected Ly$\alpha$ luminosities for all ULLYSES DR5 stars (black diamonds) as a function of total fluorescent $H_2$ luminosity. We created a power-law fit to the 14 stars with high-quality, multiprogression $H_2$ emission line data and Ly$\alpha$ reconstructions from France et al. (2012), shown as orange circles on the plot. This fit was used to predict the Ly$\alpha$ luminosity of the ULLYSES stars based on their observed $F(H_2)$.
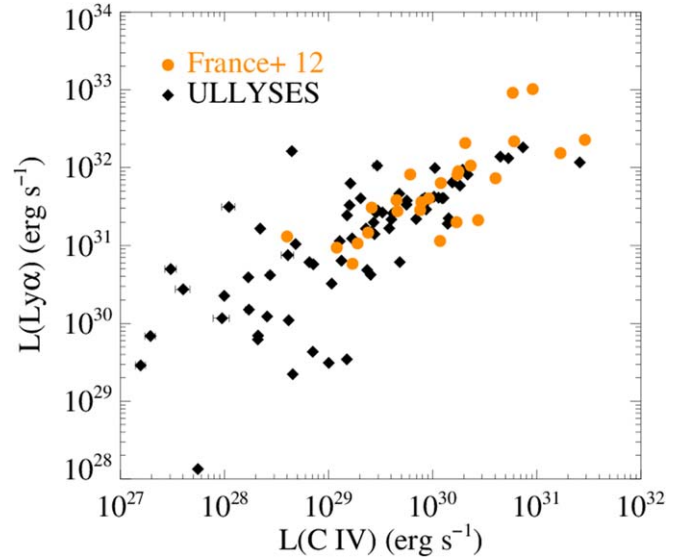


**Figure 5.** Comparison of the C IV and Ly$\alpha$ luminosities of the ULLYSES stars (black diamonds) and previous HST/COS survey of CTTSs (France et al. 2012; orange circles). The plot demonstrates the correlation between Ly$\alpha$ (as derived in Section 3.1) and accretion-dominated emission from C IV. This is consistent with the broad, bright Ly$\alpha$ profiles of CTTSs (Schindhelm et al. 2012; Arulanantham et al. 2023) being powered by mass accretion (e.g., France et al. 2014b).

the present work and the France et al. (2012) sample, showing reasonable agreement in the range $L(C\ IV) > 10^{29}$ erg s$^{-1}$ with a larger spread in the lower C IV luminosity region of the ULLYSES sample. The spread in Ly$\alpha$ values at $L(C\ IV) < 10^{29}$ erg s$^{-1}$ is driven by scatter in the relationship between C IV and $H_2$. Similarly, we find a moderate positive correlation between $L(Ly\alpha)$ and the photometric luminosity (L$_*$; from Manara et al. 2021, 2022); the Spearman rank correlation coefficient, $\rho$, and the likelihood that this correlation is

consistent with a random distribution, $n$, for the $L(\mathrm{Ly}\alpha)$ versus $L_*$ relation are $\rho = 0.498$ and $n = 2.3 \times 10^{-4}$, respectively.

### 3.2. Radial Distribution of $H_2$ Fluorescent Emission

Kinematic broadening dominates the observed $H_2$ line profiles. The thermal broadening of the emission lines is approximately 4.5 km s$^{-1}$ at the nominal 2500 K $H_2$ layer (Herczeg et al. 2004; Hoadley et al. 2015); significant additional broadening would require temperatures in excess of the $\approx$4500 K dissociation temperature of $H_2$ (Lepp & Shull 1983). If we further assume that any turbulence in the disks is subsonic, then the maximum turbulent velocity will be no larger than a few kilometers per second. Therefore, velocity broadening due to bulk motions and Keplerian rotation dominate the observed line shapes when the FWHM of the emission line is greater than the $\approx$15–20 km s$^{-1}$ spectral resolution of COS (see Figure 2; all $H_2$ lines are well resolved at the spectral resolution of HST/COS; the 1450 Å HST/COS LSF is overplotted as the green dotted line). For the case of $H_2$ in a circumstellar disk where Keplerian broadening dominates the profile, we employ a simple metric to characterize the average $H_2$ emitting radius, $\langle R_{\mathrm{H2}}\rangle$ (Salyk et al. 2011a; France et al. 2012; Arulanantham et al. 2021), where

$$\langle R_{\mathrm{H2}}\rangle_m = GM_*\left(\frac{2\sin(i)}{\mathrm{FWHM}_m}\right)^2, \qquad (4)$$

where $M_*$ is the stellar mass, $i$ is the disk inclination angle, taken primarily from Atacama Large Millimeter/submillimeter Array (ALMA) surveys (Table 1), and $\mathrm{FWHM}_m$ is the mean of the Gaussian FWHMs for a given progression $m$. When disk inclinations were not available (19/63 accreting sources), we assume a disk inclination of 60°, as this is approximately the average inclination found in ALMA disk surveys (Ansdell et al. 2018) and assumed in model studies (Rilinger & Espaillat 2021). We provide correlation coefficients for the full sample and using only the sources with known inclinations in the appropriate subsections below, and note that the "outlier" values of $\langle R_{\mathrm{H2}}\rangle$ are not driven by unknown inclinations; 5/6 of the largest $H_2$ radii presented here are for sources with measured disk inclinations. Table 1 presents the stellar masses and disk inclinations used in this work.

For the $H_2$ radial distribution analysis, we consider four progressions: the [1, 7] and [1, 4] progressions that are pumped within 100 km s$^{-1}$ of the Ly$\alpha$ line center and two progressions ([0, 1] and [0, 2]) that are pumped from the wing of the Ly$\alpha$ emission profile (379 and 487 km s$^{-1}$ from line center, respectively). We analyze multiple progressions because self-absorption can selectively impact the lower-energy level gas (Wood et al. 2002; McJunkin et al. 2016) and that off-star Ly$\alpha$ emission and the local scattering geometry can impact the flux distributions of the different progressions (Walter et al. 2003; Arulanantham et al. 2023). We will return to a discussion of these results in Section 4.

### 3.3. $H_2$ Dissociation Emission and the FUV Continuum

FUV continuum spectra were created for the ULLYSES DR5 sample following the continuum extraction methodology described in France et al. (2014b). We create a grid of 205 unique spectral points between 1138 and 1791 Å, selected by hand to avoid discrete molecular and atomic emission and
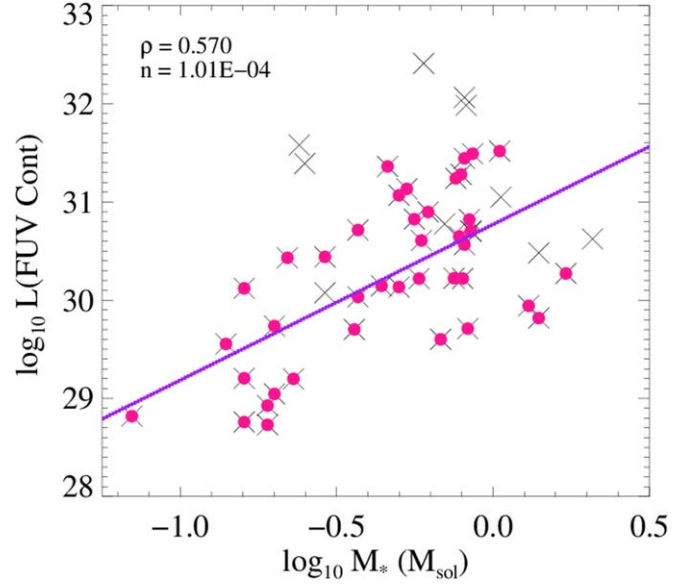


**Figure 6.** The FUV continuum luminosity increases with pre-main-sequence stellar mass. The stars in the ULLYSES sample with good measurements of the average $H_2$ emitting radius are shown with a black "x", and those with literature $A_V < 1$ are overlaid with pink circles (see Sections 3.3 and 4.1). A fit to the $A_V < 1$ points is overplotted in purple. The Spearman rank coefficient ($\rho$) and probability coefficient for null correlation ($n$) of the $A_V < 1$ points are shown at the upper left.

absorption features, where 0.75 Å (approximately 10 spectral resolution elements) spectral continuum windows can be cleanly measured. We measure the mean and standard deviation of the observed spectra, and these points define the binned flux spectrum and error array (see Figure 3). These binned spectra are then corrected for interstellar reddening and the FUV continuum and $H_2$ continuum emission (the "1600 Å Bump") are separated as described below.

We measure the FUV continuum emission by fitting the binned spectrum with a second-order polynomial at wavelengths away from the Bump, and residual stellar or airglow emission in the regions $\Delta\lambda = 1145$–1190 Å, 1245–1330 Å, 1395–1401 Å, 1420–1465 Å, 1690–1710 Å, and 1730–1750 Å (see the blue dashed lines in Figure 3). The polynomial fit is extrapolated to the atomic hydrogen ionization limit, 912 Å, to cover the primary photodissociating spectral region for $H_2$, CO, and $N_2$. Comparison with archival FUSE observations between 1000 and 1180 Å has shown that this extrapolation is a reasonably good match to the observed short-wavelength flux (France et al. 2014b). The FUV continuum flux, $F_{\mathrm{FUVCont}}$, is the integral of the polynomial over the 912–1760 Å wavelength region and the FUV continuum luminosity is defined as $L(\mathrm{FUV\ Cont}) = 4\pi d^2 F_{\mathrm{FUVCont}}$.

Figure 6 shows the FUV continuum luminosity as a function of stellar mass. We observe a positive correlation between the continuum and stellar mass ($\rho = 0.570$ and $n = 1.0 \times 10^{-4}$, as shown in the legend of Figure 6), which is expected in the scenario where the FUV continuum emission is dominated by mass accretion onto the central star (France et al. 2014b). Figure 6 plots the sources for which "good" $H_2$ radii are measured (see the discussion in Section 4.1), and it is observed that the most luminous sources are also the sources with the largest reddening ($A_V$). The attenuation toward FUV-emitting regions of protoplanetary targets has been estimated to be lower than estimates inferred from X-ray, optical, or IR

measurements (e.g., McJunkin et al. 2014). Hence, extinction values derived from, e.g., IR observations may overestimate the extinction correction for UV data. This was demonstrated by France et al. (2017), who showed that the largest $A_V$ values derived from IR-based extinctions led to unphysical correlations in FUV luminosity relationships. To avoid biasing the results by the largest, possibly incorrect, $A_V$ values, Figure 6 also shows the 41 stars with $A_V < 1$ as pink circles. The correlation coefficient and best-fit line are presented for the $A_V < 1$ sample.

The most prominent spectral feature in the binned spectra of some CTTSs is the 1600 Å Bump feature created during the dissociation of $H_2$ molecules with highly nonthermal rovibrational distributions, which spans $\sim$30–150 Å and has a peak flux $\sim$0–4 times the underlying continuum level at 1600 Å. We define the 1600 Å Bump as the excess emission above the FUV continuum in the 1490–1690 Å spectral region, where the Bump spectrum is the binned data minus the FUV continuum fit. An example of the well-defined Bump spectrum of DM Tau is shown in Figure 3. Following previous work, we parameterize the Bump emission as a broad Gaussian plus a second-order polynomial (France et al. 2017; Figure 3, bottom panel). We define the total Bump flux, $F_{Bump}$, as the integral of the continuum-subtracted Bump spectrum from 1490 to 1690 Å, and $L(1600 \text{ Å Bump}) = 4\pi d^2 F_{Bump}$.

## 4. Discussion: The Spatial Distribution and Excitation Conditions of $H_2$ Line and Continuum Emission

### 4.1. Variation of $\langle R_{H2} \rangle$ with FUV Emission and Dust Environments

The average $H_2$ line emission radius represents the characteristic Keplerian velocity of the gas, assuming the spectral broadening is dominated by the rotational motion of the disk. In a future work, we will present a more detailed line profile decomposition of a subset of bright disks to constrain stratified gas structures and wind contributions (e.g., Herczeg et al. 2006; Gangi et al. 2023), but for the full ULLYSES sample, we assume a single emission line component. The objects included in the analysis are restricted to disk inclinations $> 15°$ (the Doppler motion cannot be confidently measured for face-on disks at the resolution of HST/COS) and do not have any data quality flags (low S/N or spectral blending) in the $H_2$ emission line catalog.

The final sample of sources that meet these criteria ("good" $H_2$ radii) includes 52, 38, 39, and 31 disks in the [1, 4], [1, 7], [0, 1], and [0, 2] progressions, respectively. $\langle R_{H2} \rangle$ values range between 0.05 and 2.9 au, with average emitting radii between 0.53 and 0.72 au (median radii between 0.35 and 0.57 au) for the four progressions. The majority of the fluorescent line emission (based on the standard deviation of the radial distributions of the four progressions) arises between 0.1 and 1.4 au. This typical emitting range can be seen in the cluster of radial distributions in Figure 7. The minimum range of $H_2$ emitting radii (0.05–0.1 au) are comparable to the dust sublimation radius and the inner disk dust rim radii measured by GRAVITY (0.1–0.2 au; GRAVITY Collaboration et al. 2021), suggesting that the molecular gas and dust edges may overlap in some sources.

Figure 7 shows the relationship between $\langle R_{H2} \rangle$ and the C IV luminosity ($\rho = 0.383$ and $n = 5.6 \times 10^{-3}$, reducing to $\rho = 0.330$ and $n = 4.9 \times 10^{-2}$ if restricted to disks with
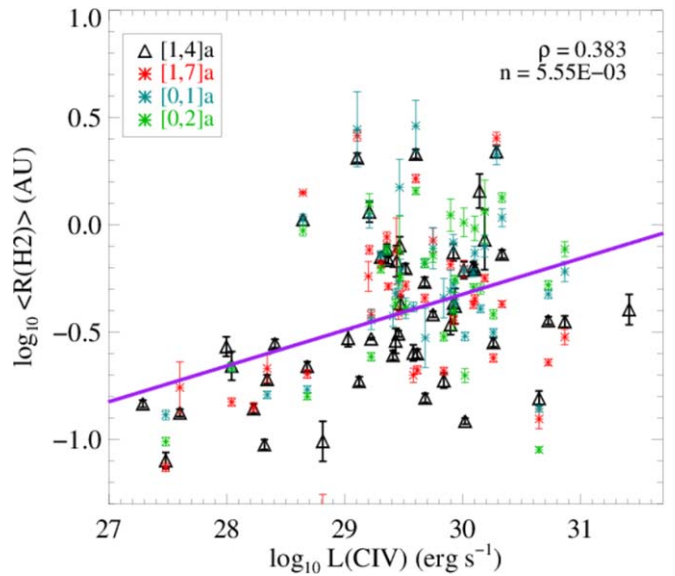


**Figure 7.** A comparison of the C IV luminosity with the average $H_2$ emitting radius for four of the progressions studied in this work (color coded as indicated in the legend). As has been shown in previous work, the majority of $H_2$ emission in CTTS systems arises between 0.1 and 3 au. The best-fit power-law relationship between $L$ (C IV) and $\langle R_{H2} \rangle$ for the [1, 4] progression is shown overplotted in purple and the Spearman rank coefficient ($\rho$) and probability coefficient for null correlation ($n$) are shown at the upper right. Assuming that C IV serves as a proxy for the accretion luminosity, the $H_2$ radial distribution demonstrates a weak dependence on the strength of the high-energy emission, possibly suggesting increased molecular dissociation in the innermost region of rapidly accreting systems.

measured inclinations). Given the variability in mass accretion rates and FUV fluxes over time (Espaillat et al. 2019; Claes et al. 2022; Hinton et al. 2022), we use the $L$(C IV) measured contemporaneously with the $H_2$ emission lines to provide a proxy for the "real-time" FUV radiation field of the central star. In Figure 7, we observe a marginal positive correlation between the emitting radius and the strength of the C IV emission. This result may indicate that higher FUV fluxes result in larger equilibrium radii with the heating/dissociating FUV radiation field (e.g., Cazzoletti et al. 2018), suggesting higher levels of $H_2$ dissociation, or the clearing of $H_2$-shielding inner disk dust, close to the central star in more FUV-luminous systems (Figure 6). We note that the lowest C IV luminosity systems ($\log_{10}(L(C IV)) \lesssim 28.7$) populate the lower left quadrant in Figure 7 ($\log_{10}\langle R_{H2} \rangle \lesssim 0.3$). Comparing the distribution of $L$ (C IV) with the stellar mass reveals that all stars with $\log_{10}(L(C IV)) \lesssim 28.7$ also have $M_* < 0.3\,M_\odot$. This supports the idea that the lowest-mass sources with the lowest $L$(C IV) show less dissociation in their innermost disks than their more massive counterparts. This would lead the stellar Ly$\alpha$ photons to encounter optically thick gas at smaller radial distances, which manifests as a small $\langle R_{H2} \rangle$ in these systems.

We observe a stronger correlation ($\rho = 0.692$ and $n = 3.2 \times 10^{-5}$) between the average $H_2$ emitting radius and the disk dust mass (Figure 8). The actual distribution is not a straight linear trend; instead, the $H_2$ emitting radii are roughly constant between $\approx$0.1–0.4 au for dust masses $\lesssim 20\,M_{Earth}$, with no $H_2$ radii larger than $\approx$0.4 au. For dust masses $\gtrsim 20\,M_{Earth}$, the $H_2$ radii range from 0.2 to 2 au. It is established that more massive stars host massive dust disks (Andrews et al. 2013; Pascucci et al. 2016; Ansdell et al. 2017) and that dust
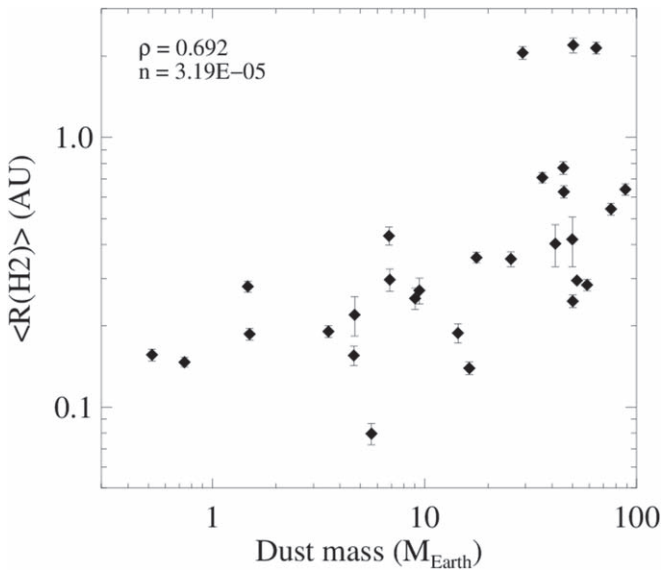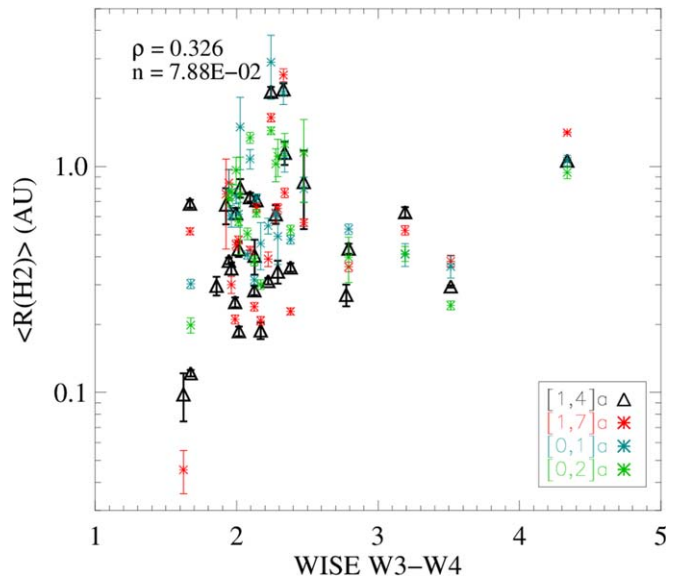
**Figure 8.** A comparison of the dust masses derived from millimeter-wave observations (see Manara et al. 2022 for a review) with the average $H_2$ emitting radius for the [1, 4] progression (29 sources had both dust masses, disk inclinations $> 15°$, and good $H_2$ FWHM observations). The Spearman rank coefficient ($\rho$) and probability coefficient for null correlation ($n$) are shown at the upper left. The behavior is consistent with a picture where more massive stars hosting more massive dust disks also photodissociate their inner few 0.1 au, leading to a correlation between disk mass and $H_2$ emitting radii.

disk mass is correlated with mass accretion rate (Manara et al. 2016; Mulders et al. 2017; Manara et al. 2022). The observation of larger gas clearing radii around stars with larger dust masses (and higher FUV continuum luminosities) is consistent with this picture of inner disk structure, as is the scenario presented above where the stars with the lowest masses (and C IV luminosities) were found to host $H_2$ populations with the smallest emitting radii.

Figure 9 displays the relationship between the WISE W3 – W4 color[18] and $\langle R_{H2} \rangle$. With the relatively low Spearman correlation coefficient ($\rho = 0.326$) and high probability of noncorrelation ($n = 0.079$), we do not find a correlation between the slope of the inner disk dust SED and the average $H_2$ emitting radius. This is in some tension with the findings of Hoadley et al. (2015), who observed a positive correlation between their modeled radial distribution of $H_2$ fluorescence and the $n_{13-31}$ dust spectral energy distribution derived from Spitzer/IRS spectroscopy. There are two key differences between these studies: first, the Spitzer data employed by Hoadley et al. (2015) are a cleaner metric of warm inner disk dust clearing than the WISE photometric points (Espaillat et al. 2014). The WISE W3 band in particular includes the 10 $\mu$m silicate emission feature seen in many CTTS spectra (Olofsson et al. 2010), and the lower angular resolution of WISE increases the possibility of source confusion. Second, Hoadley et al. (2015) employ an emission line forward-modeling analysis of a higher-S/N sample of disk targets; they find correlations between inner disk dust clearing and the maxima of the $H_2$ radial distributions derived from their models. A follow-on study of the high-S/N ULLYSES sources with Spitzer or JWST spectra would be valuable for a more direct comparison with the Hoadley et al. (2015) results.

---

[18] WISE W3 is centered at 12 $\mu$m, full band range $\sim 7.5$–16 $\mu$m; WISE W4 is centered at 22 $\mu$m, full band range $\sim 20$–25 $\mu$m; Wright et al. (2010).



**Figure 9.** A comparison of the WISE 12 – 22 $\mu$m color with the average $H_2$ emitting radius for four of the progressions studied in this work (color coded as indicated in the legend). The distribution of emitting radii are clustered between W3 and W4 $\approx 2.0$ and 2.5, respectively, with a small number of transition disks (Sz 111, DM Tau, and CS Cha) extending to large mid-IR flux ratios. The Spearman rank coefficient ($\rho$) and probability coefficient for null correlation ($n$) are shown at the upper left.

### 4.2. Inner Disk Opacity and $H_2$ Continuum Emission

There are two proposed origins for the 1600 Å Bump emission seen in many protoplanetary disk sources. The first proposes that free electrons (possibly liberated by X-ray emission from the central star) collide with the disk surface population of $H_2$, creating an electron impact spectrum similar to that observed in the aurorae of giant planets (Bergin et al. 2004; Ingleby et al. 2009). The second route for the formation of the 1600 Å Bump proposes that bright stellar+accretion-generated Ly$\alpha$ emission dissociates water molecules and that the broad continuum Bump is produced during the photodissociation of the nonthermal $H_2$ created during the breakup (dissociation) of the water molecules (van Harrevelt & van Hemert 2008; France et al. 2017).

Analysis of the ULLYSES DR5 sample finds 24 sources with detectable 1600 Å Bump emission, a detection rate of 38%, roughly consistent with the $\approx 50\%$ detection rate reported in France et al. (2017). We find a strong correlation between the strength of the Bump and the Ly$\alpha$ field strength. Figure 10 illustrates the relationship between the Ly$\alpha$ and 1600 Å Bump luminosities, where the highly significant correlation ($\rho = 0.8$ and $n = 2.7 \times 10^{-6}$) strongly suggests Ly$\alpha$ photons as central to the formation of the $H_2$ continuum emission feature. For comparison, the correlation between C IV and the 1600 Å Bump luminosity is less pronounced ($\rho = 0.5$ and $n = 1.6 \times 10^{-2}$). We also note that the Ly$\alpha$ luminosities in sources with strong Bump detections are $\gtrsim 5 \times 10^{31}$ erg s$^{-1}$, i.e., the Ly$\alpha$ region strongly anchored by the France et al. (2012) Ly$\alpha$ reconstruction sample.

Within the sample of 24 1600 Å Bump detections, 14 had WISE W3 – W4 colors without data quality warnings. We plot the Bump luminosity versus the W3 – W4 color in Figure 11. We observe a correlation ($\rho = 0.68$ and $n = 7.6 \times 10^{-3}$) between these quantities, with disks showing the largest depletion of optically thick warm dust (noting the caveats about spectral and spatial contamination in the WISE photometric bands discussed previously) having the largest $H_2$ continuum emission luminosity.
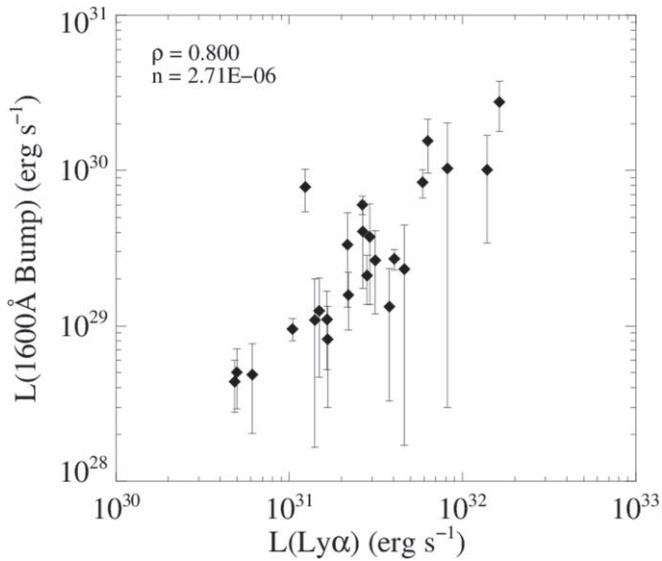
**Figure 10.** The 1600 Å Bump luminosity is strongly correlated with Ly$\alpha$ luminosity. This correlation supports the hypothesis that the Bump is powered by Ly$\alpha$-driven $H_2O$ dissociation. The Spearman rank coefficient ($\rho$) and probability coefficient for null correlation ($n$) are shown at the upper left.

Taken together with the strong correlation with $L(Ly\alpha)$, the emerging picture for the formation of the 1600 Å Bump includes both strong accretion-generated Ly$\alpha$ flux and low optical depth in the inner disk gas and dust environment. Bright Ly$\alpha$ emission alone is not a sufficient condition to produce the $H_2$ continuum emission, as there are 44 targets in our sample with $L(Ly\alpha) > 10^{31}$ erg s$^{-1}$ (including, e.g., CVSO-109, Figure 3; Espaillat et al. 2022) yet only 21 of those are detected in the 1600 Å Bump feature. The second required condition is that those Ly$\alpha$ photons are able to reach the molecular reservoirs in the inner disk. As the gas and dust opacities decline with time, Ly$\alpha$ photons can more readily reach the molecular populations of the inner disk, where they dissociate water molecules and the resultant nonthermal $H_2$ gas.

## 5. Summary

We have analyzed FUV spectra of 71 young stars included in ULLYSES DR5. We have created a uniform emission line extraction and measurement database of fluorescent $H_2$ and magnetospheric and accretion-generated hot gas lines that are hosted on a public website at the University of Colorado[19]. The $H_2$ database is used to compute the total fluorescent $H_2$ luminosity and to estimate the Ly$\alpha$ luminosity from the ULLYSES sample.

The line widths are combined with the stellar mass and disk inclination to derive the average $H_2$ emitting radius for the fluorescent emission. We find that the majority of the fluorescent emission arises between 0.1 and 1.4 au from the central star. We find a weak positive correlation between the average emitting radius and the stellar FUV flux, and a stronger correlation between the $H_2$ emitting radius and the dust disk mass. We extracted FUV continuum spectra and $H_2$ dissociation emission from the ULLYSES sample, finding 24 detections of $H_2$ continuum emission. We find strong correlations between the $H_2$ continuum emission and both the Ly$\alpha$ luminosity and the mid-IR (10–22 $\mu$m) inner disk dust slope. These results support a picture for the production of the
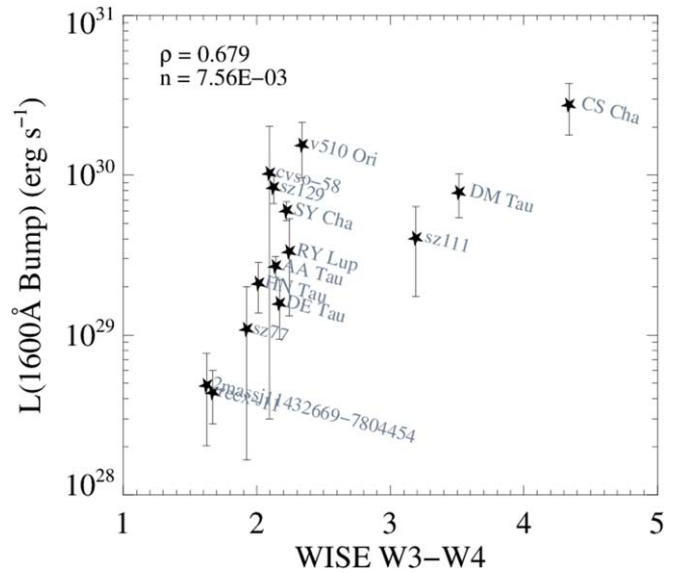


**Figure 11.** A comparison between the WISE 12 and 22 $\mu$m color and the 1600 Å Bump luminosity. Targets are labeled for reference and the Spearman rank coefficient ($\rho$) and probability coefficient for null correlation ($n$) are shown at the upper left. The positive correlation indicates that as the inner disk opacity decreases, stellar+accretion-generated Ly$\alpha$ photons can penetrate farther into the disk where they dissociate $H_2O$, creating the nonthermal $H_2$ population that gives rise to the 1600 Å molecular dissociation continuum.

$H_2$ continuum where a decrease of the inner disk gas and dust opacity enables bright stellar Ly$\alpha$ emission to reach the molecular populations of the inner disk (Bergin et al. 2003; Bethell & Bergin 2011), driving molecular dissociation and the associated continuum emission.

## ORCID iDs

Kevin France https://orcid.org/0000-0002-1002-3674
Nicole Arulanantham https://orcid.org/0000-0003-2631-5265
P. Wilson Cauley https://orcid.org/0000-0001-9207-0564
P. Ábrahám https://orcid.org/0000-0001-6015-646X
Juan M. Alcalá https://orcid.org/0000-0001-8657-095X
Justyn Campbell-White https://orcid.org/0000-0002-3913-3746
Eleonora Fiorellino https://orcid.org/0000-0002-5261-6216
Gregory J. Herczeg https://orcid.org/0000-0002-7154-6065
Brunella Nisini https://orcid.org/0000-0002-9190-0113
Miguel Vioque https://orcid.org/0000-0002-4147-3846

---

[19] https://ullyses.stsci.edu/ullyses-download.html

# References

Alcalá, J. M., Manara, C. F., France, K., et al. 2019, A&A, 629, A108
Alcalá, J. M., Manara, C. F., Natta, A., et al. 2017, A&A, 600, A20
Alcalá, J. M., Natta, A., Manara, C. F., et al. 2014, A&A, 561, A2
Alexander, R., Pascucci, I., Andrews, S., Armitage, P., & Cieza, L. 2014, Protostars and Planets VI (Tucson, AZ: Univ. Arizona Press), 475
Andrews, S. M., Rosenfeld, K. A., Kraus, A. L., & Wilner, D. J. 2013, ApJ, 771, 129
Ansdell, M., Williams, J. P., Manara, C. F., et al. 2017, AJ, 153, 240
Ansdell, M., Williams, J. P., Trapman, L., et al. 2018, ApJ, 859, 21
Ansdell, M., Williams, J. P., van der Marel, N., et al. 2016, ApJ, 828, 46
Ardila, D. R., Herczeg, G. J., Gregory, S. G., et al. 2013, ApJS, 207, 1
Arulanantham, N., France, K., Hoadley, K., et al. 2018, ApJ, 855, 98
Arulanantham, N., France, K., Hoadley, K., et al. 2021, AJ, 162, 185
Arulanantham, N., Gronke, M., Fiorellino, E., et al. 2023, ApJ, 944, 185
Balbus, S. A., & Hawley, J. F. 1991, ApJ, 376, 214
Banzatti, A., Abernathy, K. M., Brittain, S., et al. 2022, AJ, 163, 174
Banzatti, A., & Pontoppidan, K. M. 2015, ApJ, 809, 167
Banzatti, A., Pontoppidan, K. M., Pére Chávez, J., et al. 2023, AJ, 165, 72
Bergin, E., Calvet, N., D'Alessio, P., & Herczeg, G. J. 2003, ApJL, 591, L159
Bergin, E., Calvet, N., Sitko, M. L., et al. 2004, ApJL, 614, L133
Bethell, T. J., & Bergin, E. A. 2011, ApJ, 739, 78
Braun, T. A. M., Yen, H.-W., Koch, P. M., et al. 2021, ApJ, 908, 46
Brittain, S. D., Najita, J. R., & Carr, J. S. 2015, Ap&SS, 357, 54
Brown, J. M., Pontoppidan, K. M., van Dishoeck, E. F., et al. 2013, ApJ, 770, 94
Calvet, N., D'Alessio, P., Watson, D. M., et al. 2005, ApJL, 630, L185
Calvet, N., & Gullbring, E. 1998, ApJ, 509, 802
Calvet, N., Muzerolle, J., Briceño, C., et al. 2004, AJ, 128, 1294
Cardelli, J. A., Clayton, G. C., & Mathis, J. S. 1989, ApJ, 345, 245
Carmona, A., van der Plas, G., van den Ancker, M. E., et al. 2011, A&A, 533, A39
Carr, J. S., & Najita, J. R. 2011, ApJ, 733, 102
Carvalho, A. S., & Hillenbrand, L. A. 2022, ApJ, 940, 156
Cazzoletti, P., van Dishoeck, E. F., Visser, R., Facchini, S., & Bruderer, S. 2018, A&A, 609, A93
Claes, R. A. B., Manara, C. F., Garcia-Lopez, R., et al. 2022, A&A, 664, L7
Costigan, G., Vink, J. S., Scholz, A., Ray, T., & Testi, L. 2014, MNRAS, 440, 3444
Cutri, R. M., Wright, E. L., Conrow, T., et al. 2013, Explanatory Supplement to the AllWISE Data Release Products
Dodson-Robinson, S. E., & Salyk, C. 2011, ApJ, 738, 131
Donati, J. F., Hébrard, E., Hussain, G., et al. 2014, MNRAS, 444, 3220
Ercolano, B., & Owen, J. E. 2016, MNRAS, 460, 3472
Ercolano, B., & Pascucci, I. 2017, RSOS, 4, 170114
Espaillat, C., Calvet, N., D'Alessio, P., et al. 2007, ApJL, 664, L111
Espaillat, C., Muzerolle, J., Najita, J., et al. 2014, in Protostars and Planets VI, ed. H. Beuther (Tucson, AZ: Univ. Arizona Press), 497
Espaillat, C. C., Herczeg, G. J., Thanathibodee, T., et al. 2022, AJ, 163, 114
Espaillat, C. C., Robinson, C., Grant, S., & Reynolds, M. 2019, ApJ, 876, 121
Fedele, D., van den Ancker, M. E., Henning, T., Jayawardhana, R., & Oliveira, J. M. 2010, A&A, 510, A72
France, K., Herczeg, G. J., McJunkin, M., & Penton, S. V. 2014a, ApJ, 794, 160
France, K., Schindhelm, E., Bergin, E. A., Roueff, E., & Abgrall, H. 2014b, ApJ, 784, 127
France, K., Roueff, E., & Abgrall, H. 2017, ApJ, 844, 169
France, K., Schindhelm, E., Burgh, E. B., et al. 2011, ApJ, 734, 31
France, K., Schindhelm, R., Herczeg, G. J., et al. 2012a, ApJ, 756, 171
Francis, L., & van der Marel, N. 2020, ApJ, 892, 111
Frasca, A., Boffin, H. M. J., Manara, C. F., et al. 2021, A&A, 656, A138
Furlan, E., Luhman, K. L., Espaillat, C., et al. 2011, ApJS, 195, 3
Furlan, E., Watson, D. M., McClure, M. K., et al. 2009, ApJ, 703, 1964
Gangi, M., Nisini, B., et al. 2023, arXiv:2305.18940
Gangi, M., Nisini, B., Antoniucci, S., et al. 2020, A&A, 643, A32
Grant, S. L., van Dishoeck, E. F., Tabone, B., et al. 2023, ApJL, 947, L6
Green, J. C., Froning, C. S., Osterman, S., et al. 2012, ApJ, 744, 60
GRAVITY Collaboration, Perraut, K., Labadie, L., et al. 2021, A&A, 655, A73
Haisch, K. E., Jr, Lada, E. A., & Lada, C. J. 2001, ApJL, 553, L153

Hartmann, L., Herczeg, G., & Calvet, N. 2016, ARA&A, 54, 135
Hendler, N., Pascucci, I., Pinilla, P., et al. 2020, ApJ, 895, 126
Herczeg, G. J., & Hillenbrand, L. A. 2008, ApJ, 681, 594
Herczeg, G. J., Linsky, J. L., Valenti, J. A., Johns-Krull, C. M., & Wood, B. E. 2002, ApJ, 572, 310
Herczeg, G. J., Linsky, J. L., Walter, F. M., Gahm, G. F., & Johns-Krull, C. M. 2006, ApJS, 165, 256
Herczeg, G. J., Wood, B. E., Linsky, J. L., Valenti, J. A., & Johns-Krull, C. M. 2004, ApJ, 607, 369
Hinton, P. C., France, K., Batista, M. G., et al. 2022, ApJ, 939, 82
Hoadley, K., France, K., Alexander, R. D., McJunkin, M., & Schneider, P. C. 2015, ApJ, 812, 41
Huang, J., Andrews, S. M., Dullemond, C. P., et al. 2018, ApJL, 869, L42
Ingleby, L., Calvet, N., Bergin, E., et al. 2009, ApJL, 703, L137
Ingleby, L., Calvet, N., Herczeg, G., et al. 2013, arXiv:1303.0769
Ingleby, L., Calvet, N., Hernández, J., et al. 2011, AJ, 141, 127
Kenyon, S. J., & Hartmann, L. 1995, ApJS, 101, 117
Kudo, T., Hashimoto, J., Muto, T., et al. 2018, ApJL, 868, L5
Kurtovic, N. T., Pérez, L. M., Benisty, M., et al. 2018, ApJL, 869, L44
Kóspál, Á., Ábrahám, P., Diehl, L., et al. 2023, ApJL, 945, L7
Lawson, W. A., Lyo, A. R., & Muzerolle, J. 2004, MNRAS, 351, L39
Lepp, S., & Shull, J. M. 1983, ApJ, 270, 578
Lesur, G. R. J. 2021, A&A, 650, A35
Long, F., Herczeg, G. J., Harsono, D., et al. 2019, ApJ, 882, 49
Loomis, R. A., Öberg, K. I., Andrews, S. M., & MacGregor, M. A. 2017, ApJ, 840, 23
Luhman, K. L. 2004, ApJ, 617, 1216
Manara, C. F., Ansdell, M., Rosotti, G. P., et al. 2022, arXiv:2203.09930
Manara, C. F., Frasca, A., Alcalá, J. M., et al. 2017a, A&A, 605, A86
Manara, C. F., Testi, L., Herczeg, G. J., et al. 2017b, A&A, 604, A127
Manara, C. F., Frasca, A., Venuti, L., et al. 2021, A&A, 650, A196
Manara, C. F., Rosotti, G., Testi, L., et al. 2016, A&A, 591, L3
Maucó, K., Hernández, J., Calvet, N., et al. 2016, ApJ, 829, 38
McJunkin, M., France, K., Schindhelm, E., et al. 2016, ApJ, 828, 69
McJunkin, M., France, K., Schneider, P. C., et al. 2014, ApJ, 780, 150
Ribas, Á., Merín, B., Bouy, H., & Maud, L. T. 2014, A&A, 561, A54
Mulders, G. D., Pascucci, I., Manara, C. F., et al. 2017, ApJ, 847, 31
Muzerolle, J., Calvet, N., & Hartmann, L. 2001, ApJ, 550, 944
Nelissen, M., McGinnis, P., Folsom, C. P., et al. 2023, A&A, 670, A165
Öberg, K. I., & Bergin, E. A. 2021, PhR, 893, 1
Olofsson, J., Augereau, J. C., van Dishoeck, E. F., et al. 2010, A&A, 520, A39
Osterman, S., Green, J., Froning, C., et al. 2011, Ap&SS, 335, 257
Pascucci, I., Cabrit, S., Edwards, S., et al. 2022, arXiv:2203.10068
Pascucci, I., Testi, L., Herczeg, G. J., et al. 2016, ApJ, 831, 125
Pittman, C. V., Espaillat, C. C., Robinson, C. E., et al. 2022, AJ, 164, 201
Pontoppidan, K. M., Blake, G. A., & Smette, A. 2011, ApJ, 733, 84
Pontoppidan, K. M., Salyk, C., Blake, G. A., et al. 2010, ApJ, 720, 887
Rice, W. K. M., Wood, K., Armitage, P. J., Whitney, B. A., & Bjorkman, J. E. 2003, MNRAS, 342, 79
Rilinger, A. M., & Espaillat, C. C. 2021, ApJ, 921, 182
Roman-Duval, J., Proffitt, C. R., Taylor, J. M., et al. 2020, RNAAS, 4, 205
Rugel, M., Fedele, D., & Herczeg, G. 2018, A&A, 609, A70
Salyk, C., Blake, G. A., Boogert, A. C. A., & Brown, J. M. 2009, ApJ, 699, 330
Salyk, C., Blake, G. A., Boogert, A. C. A., & Brown, J. M. 2011a, arXiv:1109.4579
Salyk, C., Pontoppidan, K. M., Blake, G. A., Najita, J. R., & Carr, J. S. 2011b, ApJ, 731, 130
Schindhelm, E., France, K., Herczeg, G. J., et al. 2012, ApJL, 756, L23
Schneider, P. C., Günther, H. M., & France, K. 2020, Galax, 8, 27
Simon, M., Guilloteau, S., Beck, T. L., et al. 2019, ApJ, 884, 42
Simon, M., Guilloteau, S., Di Folco, E., et al. 2017, ApJ, 844, 158
Slesnick, C. L., Carpenter, J. M., Hillenbrand, L. A., & Mamajek, E. E. 2006, AJ, 132, 2665
van der Marel, N., Williams, J. P., Ansdell, M., et al. 2018, ApJ, 854, 177
van Harrevelt, R., & van Hemert, M. 2008, JPCA, 112, 3002
Walter, F. M., Herczeg, G., Brown, A., et al. 2003, AJ, 126, 3076
Wang, L., & Goodman, J. 2017, ApJ, 847, 11
Wood, B. E., Karovska, M., & Raymond, J. C. 2002, ApJ, 575, 1057
Wright, E. L., Eisenhardt, P. R. M., Mainzer, A. K., et al. 2010, AJ, 140, 1868